Journal of Materials Chemistry A

Accepted Manuscript

ROYAL SOCIETY OF CHEMISTRY

www.rsc.org/materialsA

Artificial Photosynthesis Using Metal/Nonmetal-Nitride Semiconductors: Current Status, Prospects, and Challenges

M. G. Kibria and Z. Mi*

Department of Electrical and Computer Engineering, McGill University

3480 University Street, Montreal, Québec H3A 0E9, Canada

**E-mail: zetian.mi@mcgill.ca, Phone: +1 514 398 7114*

Abstract: Artificial photosynthesis, i.e. the chemical transformation of sunlight, water and carbon dioxide into high-energy-rich fuels is one of the key sustainable energy technologies to enable carbon-free, storable and renewable source of energy. Although significant progress has been made over the last four decades, the development of efficient, long-term stable, scalable, and cost-competitive photocatalysts has remained one of the key challenges for the large-scale practical application of this frontier technology. Over the last decade metal/nonmetal-nitrides have emerged as a new generation of photocatalyst materials for artificial photosynthesis owing to their distinct optoelectronic and catalytic properties. This article provides an overview of the state-of-the-art research activities on the development of metal/nonmetal-nitride semiconductor based photocatalysts and photoelectrodes for solar-fuel conversion.

Key words: Artificial photosynthesis, solar water splitting, photocatalyst, nitrides, CO_2 reduction

Introduction

Amongst various sustainable energy options, solar energy may be the ultimate solution to mitigate the current and future global energy demand.[1] The currently available photovoltaic cells can convert sunlight to electricity with an efficiency up to 46%.[2] However, because of the intermittency and variable atmospheric conditions, the major challenge remains in storing solar energy for short and long-term applications.[3] At present, there are four forms of technologies available to store energy, including (1) potential energy in the form of pumped-hydroelectric, compressed air, electric charge in super/ultra capacitors, (2) kinetic energy mainly in the form of flywheels, (3) thermal energy in the form of concentrated solar thermal, geothermal, and (4) chemical energy in the form of batteries or fuels.[3] Unfortunately, all of the present energy storage technologies experience one or more of the key obstacles, including high cost, short time storage, and low energy density to be implemented for sustainable and large-scale applications.[3] Alternatively, a potentially viable technology for solar energy storage is artificial photosynthesis, which refers to any scheme that mimics natural photosynthesis by which green plants convert sunlight, carbon dioxide (CO_2) and water into carbohydrates to capture and store solar energy in the chemical bonds of a fuel (solar-fuel).[4-9] There are commonly two schemes of artificial photosynthesis, including sunlight driven water splitting into hydrogen (H_2) fuel, and photoinduced CO_2 reduction into various hydrocarbons.[5, 9] To date, research efforts on artificial photosynthesis are mostly directed towards sunlight-driven water splitting.[10] Although H_2 is an important fuel and chemical feedstock with the highest energy density by mass (~140 MJ/Kg), it suffers from low volumetric energy densities. A practical alternative is hydrocarbon fuel with optimum volumetric energy density for better integration with existing energy infrastructure.[3] Although there is an immense potential, major challenge remains in developing a cheap, efficient and stable artificial photosynthesis system that is capable of producing cost-competitive fuels (i.e., hydrogen, methanol etc.) to replace fossil fuels.

In an artificial photosynthesis system, dye molecule or semiconductor photocatalyst captures solar energy and subsequently splits water into its constituents (i.e., H_2 and O_2) with a positive change in Gibbs free energy (i.e., uphill reaction):[11]

$$H_2O \rightarrow 1/2O_{2(g)} + H_{2\,(g)},\ \Delta G=+237.178\ KJ/mol \qquad \text{.....} (1)$$

The hydrogen produced from this reaction can be the central energy carrier in a Hydrogen Economy.[12, 13] Alternatively, this renewable hydrogen could be used to reduce anthropogenic CO_2 for the exothermic formation of useful energy-rich hydrocarbons i.e., methane, formic acid, methanol etc. These renewable value-added hydrocarbons can replace conventional fuels used for transportation or can be used as the basic synthetic components for hundreds of chemicals.[9, 14-16]

While the concept of artificial photosynthesis was envisioned and proposed in 1874 by Verne (available at http://www.literature-web.net/verne/mysteriousisland,1874), and in 1912 by Ciamician[17], respectively, the experimental demonstration was not reported until late 60's. In 1968 Boddy reported light-driven oxygen evolution at an *n*-type rutile (TiO_2) electrode.[18] Subsequently, in 1972 Fujishima and Honda applied this concept for water photoelectrolysis in a cell comprising of an *n*-type rutile (TiO_2) photoanode and a platinum cathode.[19] On the other hand, the two earliest reports on light-driven CO_2 reduction are Halmann's work on photoelectrochemical CO_2 reduction in 1978,[20] and Honda and co-workers' work on photocatalytic CO_2 reduction in 1979.[21] These seminal works stimulated decades of international effort on the development of various efficient, stable and cost-effective photocatalysts for sunlight-driven water splitting and CO_2 reduction.

Photocatalytic (also known as photochemical, Schottky-type, suspended photocatalyst or photoparticle system) and photoelectrochemical (photoelectrode system) are the two common schemes for solar-driven water splitting and CO_2 reduction. In a photocatalytic water splitting approach, the light absorption, charge carrier separation, and catalytic reactions proceed on an integrated photosystem, consisting of a host photocatalyst and one or more co-catalysts.[22] The ideal limiting solar-to-hydrogen (STH) efficiency of such an integrated photosystem is 14.4% (single-bandgap photosystem), assuming a bandgap of 2.0 eV and energy loss of 0.8 eV per electron.[23] A 10% STH efficiency in photocatalytic system would provide H_2 at a cost of \$1.63/Kg, providing a cost-competitive alternative to gasoline.[24] To date researches have been largely

focused on metal-oxide based photocatalysts owing to their photostability in aqueous solution.[10, 11, 25] However, most of the metal-oxides suffer from inefficient light absorption (max limiting STH efficiency of ~2.3%) due to their large bandgap (O2p orbital locates at ca. +3.0 eV or higher) and/or poor optoelectronic properties, i.e., their short electron-hole lifetimes and low mobility.[26] Therefore, a number of band-engineering and nanostructuring strategies have been developed to overcome the limiting factors of metal-oxides, including metal/nonmetal ion doping (e.g., C^{4-}, N^{3-}, and S^{2-}), solid solution (GaN:ZnO, quantum efficiency=5.9%), elemental substitution, sensitization etc.[27-31] However, owing to inefficient light absorption and limited carrier extraction, the achieved STH efficiency (<0.1%) of such band-engineered photocatalyst is far below the values of practical interest (~10%). Although relatively high STH efficiencies (e.g., 5% from CoO,[32] 2% from CDots-C_3N_4,[33] and 1.8% from p-GaN/p-InGaN[34]) have been reported by combinatorial approaches very recently, their long-term instability and high cost remain the key concerns for commercialization. Alternatively, a Z-scheme (also known as tandem or two-step photoexcitation system) photosystem has been developed to utilize a wide variety of small bandgap materials.[35-37] In this system, two or more photoabsorbers are connected via a redox shuttle. While the ideal limiting STH efficiency of such a Z-scheme is relatively high (24.4% for bandgaps of 2.25 and 1.77 eV),[23] the achieved STH efficiency to date is extremely low (~0.1%) due to greater system complexity.[38]

In the scheme of photoelectrochemical (PEC) water splitting, the oxidation and reduction reactions proceed on two different electrodes that are connected via an external circuitry.[39] In this case, some external bias is usually required for efficient carrier separation and to overcome the resistance between the electrodes in the solution. As the light absorption, charge separation, and catalytic reactions do not proceed at close proximity, PEC water splitting is more complex and is nearly one order of magnitude more expensive than photochemical system at equal efficiency.[40] To date the reported STH efficiencies of metal-oxide and other semiconductor-based photoelectrodes are low due to inefficient light absorption, limited carrier separation, and insufficient redox potentials.[31, 41] To overcome the efficiency bottleneck and reduce the cost, photovoltaic (PV) integration with PEC system (PV+PEC) or with electrocatalyts (PV+EL) has achieved

impressive success, with STH efficiencies from 3 to 22%.[42, 43,44,45,46, 47-52] While the achieved efficiency is over half of the theoretical efficiency limit of these devices (i.e., 24.4% for a tandem and 30% for multi-junction),[23, 53, 54] the long-term instability of the photoabsorbers, and their limited scalability due to high cost remain some of the major concerns.[55] Therefore, a number of stable passivation materials (e.g., TiO_2, Ir/TiO_2, Ni, $SrTiO_3$, MnO etc.) have been developed to enhance the stability of Si and III-V; however, with limited success.[56-60]

In the meantime, research on metal/nonmetal-nitride photocatalysts and photoelectrodes (e.g., GaN, InGaN, C_3N_4, T_3N_5, Ge_3N_4, W_2N, InN, BCN etc.) for water splitting has drawn considerable attention. Illustrated in Fig. 1, publications in this field have increased exponentially in the last decade. This rapid rise has been fuelled, to a certain extent, by the recent development of LED lighting technology, which has led to significantly improved material quality of metal-nitride semiconductors with dramatically reduced manufacturing cost.[61] Tables 1-2 summarize the major works on metal/nonmetal-nitride based photocatalysts and photoelectrodes for solar water splitting. Metal/nonmetal-nitrides possess excellent catalytic, electrical and optical properties. For example, metal/nonmetal-nitride semiconductors often possess a narrow band gap due to the more negative potential of the N2p orbital compared to the O2p orbital in metal-oxides.[62] As an example, the bandgap of metal-oxide Ta_2O_5 is 3.9 eV, whereas the bandgap of Ta_3N_5 is 2.1 eV.[63] As illustrated in Fig. 2, the bandgap of most of the metal/nonmetal-nitrides straddle the redox potential of water, with sufficient kinetic overpotentials for water redox reactions and CO_2 reduction to various hydrocarbons. In contrast, most of the metal-oxides do not possess suitable conduction band edge required for water (or CO_2) reduction to hydrogen (or hydrocarbons).[10] One of the nitrides, GaN, possesses a direct energy bandgap that can be tuned from 3.4 to 0.65 eV across the ultraviolet, visible, and near-infrared spectrum by introducing indium (In),[64, 65] thereby offering the unique opportunity to harness nearly the entire solar spectrum.[66] Additionally, nitrides possess high absorption co-efficient and large charge carrier mobility, leading to excellent photon absorption and charge carrier extraction for efficient solar-fuel conversion.[65, 67, 68] In contrast to traditional III-V compounds, wherein the chemical bonds are mostly covalent, the chemical bonds

in III-nitrides are strongly ionic.[69] Because of the strong ionicity of nitrides, the surface states are located mostly near the band edges, which prevent them from being non-radiative recombination centers. Consequently, the Fermi level is not pinned in the energy gap of III-nitrides, thereby suppressing the participation of these states in self-oxidation process of photoanode, resulting in photostability of the electrode.[69] However, the presence of any surface defects, which often depends on the growth method, may lead to Fermi-level pinning in the bandgap and photodegrade the material. Indeed, recent studies have demonstrated excellent photostability of nearly defect-free metal-nitrides against photocorrosion in acidic and neutral pH electrolyte.[70-72] Therefore, it is suggested that defect-free and high crystalline quality nitrides can function both as anode and cathode. However, in the presence of high density of defects, nitrides may be more suitable as photocathode.[73]

In an effort to improve the performance of blue LEDs, the epitaxial growth technique of high crystalline quality III-nitrides has been substantially improved in early-90's.[61] Subsequently, in 1995, John Turner and co-workers demonstrated that high quality metal-nitride (*n*-GaN) functioned as a viable photoelectrode material for solar water splitting.[74] Detail photoelectrochemical characterization reveals that the bandgap of GaN straddles the redox potential of water with sufficient overpotentials, such that photolysis of water is possible on GaN without external bias.[75-79] This work triggered the development of various nitride-based photocatalysts and photoelectrode materials (i.e., InGaN, T_3N_5, Ge_3N_4, and W_2N) over the years. In 2009, a cheap, stable and earth abundant nonmetal nitride, i.e., polymeric carbon-nitride has been developed by Antonietti's group, which can produce hydrogen from water under visible light irradiation.[80] This seminal work has opened a new avenue for further research on carbon-nitrides to function as a viable catalyst for solar water splitting and CO_2 reduction to energy rich hydrocarbons under visible light irradiation. In recent years, metal/nonmetal-nitrides in the form of nanostructures have been investigated by a number of research groups because of their excellent structural, optical and catalytic properties over their bulk counterparts.

Given the rapid development of nitride based photocatalysts and photoelectrodes for artificial photosynthesis, there is clearly an urgent need to provide a comprehensive overview of the recent progress

and research activities in this area. Unlike other review articles,[10, 25, 31, 39, 73, 81-83] this article focuses only on metal/nonmetal-nitride based photocatalysts and photoelectrodes for solar powered artificial photosynthesis, including photocatalytic and photoelectrochemical water splitting and CO_2 reduction. The rest of the article is organized as follows. First, the mechanism of solar water splitting is briefly discussed. Photocatalytic water splitting using UV and visible light sensitive metal/nonmetal-nitrides are then summarized. Subsequently, a discussion on efficiency enhancement in photocatalytic water splitting is provided. This is followed by a summary of photoelectrochemical water splitting using UV and visible light sensitive metal/nonmetal-nitrides. Photocatalytic and photoelectrochemical CO_2 reduction using metal/nonmetal-nitrides are then discussed. Finally, the future prospects and challenges of nitrides for artificial photosynthesis are presented.

Solar water splitting: Mechanism

The fundamental processes involved in solar water splitting reaction are shown in Fig. 3. The initial step involves the absorption of incident photons and the generation of electron–hole pairs. Depending on the carrier lifetime, diffusion length, crystalline quality and photocatalyst dimension, photogenerated carriers can either recombine radiatively/nonradiatively or they can diffuse toward the semiconductor-liquid interface to drive the redox reaction. Any defects can act as trapping and recombination centers between photogenerated electrons and holes, resulting in a decrease in the photocatalytic activity. The physical size of the photocatalyst also determines the activity of the photocatalyst. If the size is small, the photogenerated carriers will travel less distance to reach the surface and hence there will be less probability of carrier recombination.[73] The use of nanostructures can thus significantly improve the performance of photocatalysts having short carrier lifetime and low mobility[73, 84, 85]. Furthermore, the near-surface band structure also plays a critical role in charge carrier extraction, as discussed in the later part of this article. The final step involves the reduction and oxidation (redox) of water on the photocatalyst surface via the photogenerated electrons and holes, respectively. The overall water splitting (i.e., simultaneous oxidation and reduction of water) consists of two half-reactions, i.e., oxygen evolution reaction (OER) and hydrogen evolution reaction

(HER).[39] The OER is essentially the first step in water splitting reaction. It oxidizes water to form O_2, described by Eqn. (2) below.

$$2H_2O \leftrightarrow O_2 + 4e^- + 4H^+, \quad E_{anodic} = 1.23\ V - 0.059\ (pH)\ V\ (NHE) \qquad \text{.....(2)}$$

Since this reaction requires a high oxidizing potential, +1.23 V vs. NHE (pH=0), the valence band maximum (VBM) has to be positioned at more positive potential than +1.23 vs. NHE (pH=0). This reaction releases four protons (H^+), which are reduced by the photogenerated electrons in HER (Eqn. 3).[39]

$$4H^+ + 4e^- \leftrightarrow 2H_2, \quad E_{cathodic} = 0\ V - 0.059\ (pH)\ V\ (NHE) \qquad \text{.....(3)}$$

Therefore, the conduction band minimum (CBM) of the semiconductor has to be positioned at more negative potential than 0 V vs. NHE at pH=0. The theoretical minimum band gap for water splitting is 1.23 eV, which corresponds to light wavelength of ~1000 nm. In practice, however, the overall bandgap requirement raises to 1.5-2.5 eV to provide sufficient kinetic overpotentials to overcome entropic losses, OER and HER overpotentials, and other parasitic losses.[39] Kinetically and energetically the OER is much more complex and slower than HER as it requires multiple intermediate steps involving four photons.[86, 87] As a result, water oxidation, i.e., the primary reaction required for H_2 production, is often the bottleneck that presents a significant difficulty in the development of an efficient catalyst. Kinetically, water oxidation process competes with fast e-h bulk recombination, fast e-h surface recombination, surface O_2 adsorption, and self-oxidation of the photocatalyst.[86]

In addition to the bandgap and band edge requirements, long-term stability of the photocatalyst in aqueous solution (in dark and under illumination) as well as the cost and material availability are the key requirements. Furthermore, HER and OER co-catalysts often need to be incorporated on the photocatalyst surface to reduce the overpotentials required for enhanced photocatalytic activity.[88] In this regard, a number of nitride based stable and efficient co-catalysts or electrocatalysts have been developed very recently, such as $NiMoN_x$[89], Ni_3N[90], $Co_{0.6}Mo_{1.4}N_2$[91], and W_2N[92].

Photocatalytic water splitting using metal/nonmetal-nitrides

A number of UV and visible light responsive metal/nonmetal-nitrides have been developed in the last decade for photocatalytic water splitting, including UV light sensitive germanium nitride (β-Ge_3N_4) and GaN, and visible light sensitive InGaN, carbon nitride (g-C_3N_4) and Ta_3N_5. The following sections provide an overview of the recent progress on UV and visible light sensitive metal/nonmetal-nitride photocatalysts for photocatalytic water splitting.

UV-light responsive metal/nonmetal-nitride photocatalysts

Sato *et al.* reported the first example of nitride photocatalyst i.e., β-Ge_3N_4 for overall water splitting in 2005.[93] It was demonstrated that RuO_2 nanoparticle dispersed β-Ge_3N_4 photocatalyst successfully decomposed water into H_2 and O_2 under UV light. Density functional theory (DFT) calculations suggested that the valence band of β-Ge_3N_4 consisted of N2p orbitals, and the photoexcited holes in such orbitals were able to oxidize water to form O_2 without requiring OER co-catalyst. The RuO_2 nanoparticles served as an active HER co-catalyst to accelerate the overall water splitting. Stable photocatalytic activity of β-Ge_3N_4 in acidic solution (1M H_2SO_4) was further confirmed by Domen's group.[94] Subsequently, by reducing the density of defects via high-pressure ammonia treatment, a 4-fold enhancement in photocatalytic activity of β-Ge_3N_4 was observed.[95] The observation of overall water splitting using a nitride based β-Ge_3N_4 photocatalyst

Table 1: A brief summary of photocatalytic water splitting using metal/nonmetal-nitrides listed in chronological order.

Photocatalyst	Co-catalyst	Light source	Reaction solution	Activity (μmol/hr/g)		Efficiency (%)	Ref. (year)
				H_2	O_2		
BCN	Pt, RuO_2, IrO_2, Ni-Co LDH	300 W Xe	Triethanolamine $AgNO_3$	80	11	AQE=0.54 (405 nm)	154 (2015)
CDots-C_3N_4		300 W Xe	Pure water	575	287	STH=2%	33 (2015)
p-InGaN/*p*-GaN	Rh/Cr_2O_3	300 W Xe	Pure water	3.46 mol/hr/g	1.69 mol/hr/g	STH=1.8%	34 (2015)
InGaN/MC-540	Rh	300 W Xe	Acetonitrile and EDTA	65 mmol/hr/g		AQE=0.3% (525-600 nm)	119 (2015)
GaN:Mg	Rh/Cr_2O_3	300 W Xe	Pure water	4 mol/hr/g	2 mol/hr/g	IQE=51%	155 (2014)
g-C_3N_4	3 wt% Pt	≥420 nm	Triethanolamine	3327		AQE=26.5% (400 nm)	150 (2014)
Conjugated C_3N_4	3 wt%	≥420 nm	10 v% triethanolamine	14800		AQE=8.8% (420 nm)	141 (2014)
$(Ga_{0.82}Zn_{0.18})(N_{0.82}O_{0.18})$ nanostructure	$Rh_{2-x}Cr_xO_3$	>400 nm	H_2SO_4 (pH 4.5)	1271	635.5	AQE=17.3% (400 nm)	109 (2014)
mpg-C_3N_4 Dye-sensitized C_3N_4 nanosheet	1.25 wt% Pt	≥420 nm	5 v% triethanolamine	6525		AQE=33.4 % (460 nm)	153 (2013)
InGaN/GaN	Rh/Cr_2O_3	300 W Xe	Pure water	92 mmol/hr/g	46 mmol/hr/g	AQE=1.86% (395-405 nm)	118 (2013)
Ta_3N_5	2 wt% CoO_x	≥420 nm	0.01 M $AgNO_3$		4500	AQE=5.2% (500-600 nm)	124 (2012)
Hollow C_3N_4 nanospheres	3 wt% Pt	>420 nm	10 v% triethanolamine	11,200		AQE=7.5% (420 nm)	133 (2012)
g-C_3N_4	1wt% RGO, 1.5% Pt	>400 nm	25% methanol	451		AQE=2.6%	151 (2011)
GaN nanowire	Core/shell Rh/Cr_2O_3	300 W Xe	Pure water	3.6	1.8	AQE=0.5%	101 (2011)
g-C_3N_4	3 wt% Pt	>420 nm	10 v% triethanolamine	~110		AQE=0.1% (420-460 nm)	80 (2009)
$(Ga_{0.82}Zn_{0.18})(N_{0.82}O_{0.18})$	$Rh_{2-x}Cr_xO_3$	>400 nm	H_2SO_4 (pH 4.5)	3090	1533	AQE=5.9 (420-440 nm)	108 (2008)
GaN powder	$Rh_{2-x}Cr_xO_3$	450 W Mercury	H_2SO_4 (pH 4.5)	64	32	AQE=0.7% (300-340 nm)	99 (2007)
GaN powder (Mg, Zn, Be doped)	RuO_2	450 W Mercury	Pure water	750	375		98 (2007)
β-Ge_3N_4	RuO_2	450 W Mercury	1M H_2SO_4	3.6 mmol/hr/g	1.8 mmol/hr/g		94 (2007)
β-Ge_3N_4	RuO_2	450 W Mercury	H_2SO_4 (pH 0)	1 mmol/hr	0.5 mmol/hr	AQE=9% (300 nm)	93 (2005)

triggered further investigations on other nitride photocatalysts. Between 2005-2007, a number of reports demonstrated the thermodynamic and kinetic potentials of GaN for overall water splitting,[76-79, 96-99] which

supports John Turner's observation[74] in 1995. Stable and stoichiometric decomposition of H_2O into H_2 and O_2 was demonstrated on GaN particulate sample decorated with either RuO_2 or $Rh_{2-x}Cr_xO_3$ HER co-catalysts.[96, 99] Interestingly, no OER co-catalyst was required for stoichiometric decomposition of water, suggesting that the surface of nitrides is inherently an active catalyst for OER reaction. Further studies on GaN showed that divalent metal ion (Mg^{2+}, Zn^{2+}, and Be^{2+}) doping significantly improved the stability and activity of GaN for overall water splititng.[98]

On the other hand, the development of heterogeneous nanostructured photocatalysts has attracted tremendous attention in the last two decades owing to their immense potential for solar-fuel production, such as efficient light absorption, large reaction surface area, efficient charge carrier extraction, higher solubility, reduced recombination, and tunable electronic band structure.[73, 84, 85, 100] Because of these unique opportunities, a number of metal-nitride nanostructured photocatalysts have been developed recently. Plasma-assisted molecular beam epitaxially (MBE) grown GaN nanowires on Si substrate have been utilized for photocatalytic water splitting, for the first time, by the authors' group.[101] The Rh/Cr_2O_3 core/shell nanoparticle decorated GaN nanowires successfully dissociated neutral pH water into H_2 and O_2 in stoichiometric ratio under full arc illumination. Compared to GaN particulate and thin film samples, significantly enhanced photocatalytic activity of GaN nanowire was observed. This enhanced activity was attributed to the large surface-to-volume ratio of one-dimensional nanowires and significantly reduced defect densities. Additionally, it was revealed that the well-defined nonpolar $(10\bar{1}0)$ surface of GaN nanowire is catalytically stable and active compared to their polar counterpart.[102] Muckerman's group studied the nonpolar $(10\bar{1}0)$ surface of GaN using ab initio molecular dynamics simulation (AIMD), and found that the nonpolar $(10\bar{1}0)$ GaN surfaces were very reactive for spontaneous dissociation ($H_2O \rightarrow H^+ + OH^-$) of majority (~83%) of the water molecules.[102, 103] In contrast, many experimental and theoretical studies suggest that water molecules do not dissociate on the photoactive TiO_2 anatase (101) and rutile (110) surfaces.[104-106] Moreover, the AIMD study revealed that the photogenerated holes on nonpolar $(10\bar{1}0)$ GaN surfaces had sufficient standard free-energy to drive the four-step water oxidation reaction.[102] In addition, the low

effective free-energy barrier for proton diffusion on GaN $(10\bar{1}0)$ surface facilitates enhanced migration of protons from the O_2 evolution reaction sites to H_2 evolution sites; therefore improves the efficiency.[107]

Photocatalytic activity of GaN nanowires grown by Ni catalyst-assisted metal-organic chemical vapor deposition (MOCVD) has also been reported.[71] Such GaN nanowires showed better activity in photodegrading dye solution compared to GaN submicron dots or thin films owing to the larger surface area and better crystallinity of the nanowires. Stable and enhanced photocatalytic activity of GaN nanowires was observed in acid pH, with much better performance than TiO_2 and ZnO nanowires. Because of the large bandgap of β-Ge_3N_4 (3.8 eV) and GaN (3.4 eV), only UV light can be harnessed, which consists of ~ 4% of the solar spectrum. As a result, significant research efforts have been devoted to developing visible light sensitive and efficient metal/nonmetal-nitride photocatalysts.

Visible-light responsive metal/nonmetal-nitride photocatalysts

In an effort to extend the light absorption of UV light sensitive wurtzite GaN and ZnO, Domen's group developed a solid solution of GaN and ZnO $(Ga_{1-x}Zn_x)(N_{1-x}O_x)$ with an absorption edge at ~510 nm.[29] The $Rh_{2-y}Cr_yO_3$ HER co-catalyst decorated solid solution $(Ga_{1-x}Zn_x)(N_{1-x}O_x)$ demonstrated successful dissociation of water under visible light (up to ~510 nm) with an apparent quantum efficiency (AQE) of 2.5% at 420-440 nm. In a follow-up study, an AQE of 5.9% at 420-440 nm was demonstrated by post-calcination treatment of as-synthesized $(Ga_{1-x}Zn_x)(N_{1-x}O_x)$ solid solution.[108] Recently, by forming nanostructures of $(Ga_{1-x}Zn_x)(N_{1-x}O_x)$, an AQE of 17.3% at 400 nm was demonstrated by Li *et al*.[109] The reduced bandgap of the solid solution is attributed to the p-d repulsion (i.e., N2p-Zn3d), which causes the top of the valence band formed by N2p atomic orbitals with higher potential energy.

Kibria *et al.* demonstrated a viable defect-engineering approach to extend the absorption edge of GaN nanowires up to 450 nm using Mg doping.[110] In order to reduce the bandgap, nitrogen vacancy related donor states and Mg impurity related acceptor states were simultaneously introduced in the bandgap of GaN nanowires during the epitaxial growth process, illustrated in Fig. 4. Using such Mg-doped GaN nanowires,

successful overall neural water splitting was demonstrated under violet light with intra-gap excitation up to 450 nm. An energy conversion efficiency of ~1.34% was demonstrated under violet light (375-450 nm).

Illustrated in Fig. 2, the bandgap of GaN can be tuned from 3.4 to 0.65 eV by introducing In, providing a viable approach to capture visible and near-infrared solar spectrum. Recent DFT studies have shown that the conduction and valence band edge of InGaN can straddle the water redox potentials for In compositions up to ~ 50%, which suggests that photocatalytic overall water splitting can be possibly realized under red and even near-infrared light irradiation.[66] However, the growth of high crystalline quality InGaN with high In content has been extremely challenging for a number of reasons.[111, 112] For instance, the large lattice mismatch (11%) between InN and GaN results in solid phase miscibility gap,[113] and the high vapor pressure of In over Ga leads to low In incorporation in InGaN.[112] Additionally, the difference in formation enthalpies between InN and GaN causes strong In surface segregation, which creates In rich clusters.[114] These factors lead to a large number of non-radiative recombination centers and strong carrier localization, which limit the photocatalytic performance of InGaN. Furthermore, TEM studies on InGaN/GaN quantum wells reveal the presence of misfit dislocations in InGaN, when InGaN is grown beyond a critical thickness.[115] This critical thickness decreases drastically with increasing In content. Therefore, the realization of high crystalline quality and high In content InGaN with sufficient thickness for efficient light absorption is quite challenging.[116] For these reasons, there have been very few studies on the photocatalytic activities of InGaN. Among different growth techniques, MBE promises to grow In-rich InGaN with superior crystalline quality.[112] Recently, the author's group has achieved nearly defect-free metal-nitride nanowires by PAMBE to function as a visible light active photocatalyst.[117] By performing OER and HER half reactions in the presence of respective sacrificial reagents, Kibria *et al.* demonstrated the thermodynamic and kinetic potentials of InGaN nanowires for overall water splitting with In compositions up to 32%.[118] The bandgap tunability of metal-nitrides from 6.2 eV (AlN) to 0.65 eV (InN) combining with the epitaxial growth of nearly defect-free nanowire structures allows for developing monolithically integrated multi-band nanowire photocatalysts to minimize the thermalization loss of energetic electrons.[23] None of the previously reported photocatalysts can function as a

single material platform to harness effectively the solar spectrum using a multi-band approach. In this context, Kibria *et al.* developed triple-band InGaN/GaN nanowires with bandgaps of 3.4, 2.96, and 2.22 eV, which led to overall neutral pH water splitting under UV, blue, and green light irradiation (up to 560 nm), illustrated in Fig. 5.[118] A maximum AQE of ~1.86% was demonstrated for overall neutral water splitting at 400 nm. Further extension of the absorption edge to deep-visible and near-infrared requires the growth of high (>40%) In content InGaN. As an alternative approach, Kibria *et al.* developed dye-sensitized InGaN nanowires to extend the solar absorption in the deep-visible spectrum.[119] It was demonstrated that Merocyanine-540 dye-sensitized and Rh nanoparticle incorporation on $In_{0.25}Ga_{0.75}N$ nanowire arrays (absorption edge ~500 nm) can produce hydrogen from ethylenediaminetetraacetic acid (EDTA) and acetonitrile mixture solution under green, yellow and orange light irradiation (up to 610 nm). An AQE of 0.3% was demonstrated in the wavelength range of 525-600 nm, providing a viable approach to harness deep-visible and near-infrared solar energy for efficient and stable water splitting.

In the year of 2002, Domen's group reported a promising visible light (<590 nm) active transition metal-nitride semiconductor i.e., Ta_3N_5; the bandgap (2.1 eV) of which is well positioned to straddle the redox potential of water.[120, 121] Hydrogen or oxygen generation under visible light in the presence of respective sacrificial reagent confirmed the thermodynamic and kinetic potentials of Ta_3N_5 for HER and OER. While Ta_3N_5 has been utilized as an O_2 evolution photocatalyst in a two-step Z-scheme photosystem[122], overall water splitting has not been reported in a Ta_3N_5 based single-step photosystem to the best of our knowledge. To date the reported quantum efficiency of Ta_3N_5 photocatalyst is still very low, despite its near-perfect band edge position and visible light absorption.[123] This is attributed to the fact that the commonly used thermal nitridation process of oxide precursor (Ta_2O_5) leads to insufficient crystallization with the presence of extensive charge recombination centers, thereby limiting the quantum efficiency. In order to improve the performance of Ta_3N_5, Domen's group modified the surface of the starting precursor (Ta_2O_5) with a small amount of Alkali metal salt.[124] Compared to conventional nitridation derived Ta_3N_5, Ta_3N_5 nitrided from Alkali metal salt (Na_2CO_3) modified Ta_3N_5 exhibited higher crystallinity and smaller particles; demonstrating

a 6-fold improvement in the photocatalytic activity for O_2 evolution under visible light. By incorporating CoO_x OER co-catalysts, an AQE of 5.2% at 500-600 nm was reported for O_2 half reaction. Very recently, Chen *et al.* demonstrated that a MgO nanolayer (2-5 nm) surface coating not only improves the interfacial contact between hydrophilic CoO_x co-catalyst and hydrophobic Ta_3N_5, but also decreases the defect density of Ta_3N_5 through a passivation effect.[125] This interface engineering significantly improves interfacial charge transfer, leading to a relatively high AQE of 11.3% at 500-600 nm for O_2 half reaction.

More recently, the use of nonmetal-nitrides for solar-fuel generation has also been studied. Wang *et al.* demonstrated the first example of visible light sensitive metal-free nitride as a new material platform to enable earth-abundant photocatalyst for water splitting.[80] Graphitic carbon nitride (g-C_3N_4) was synthesized by thermal polycondensation of common organic monomers, illustrated in Fig. 6. The g-C_3N_4 is soft polymeric nitride with conjugation structure and possesses very high thermal and chemical stability, and excellent optoelectronic properties, including a direct energy bandgap of 2.7 eV, which straddles the redox potential of water, as shown in Fig. 2.[126, 127] The g-C_3N_4 photocatalyst showed stable photocatalytic activity to generate H_2 from water under visible light (up to 540 nm) in the presence of electron donors without using any noble metal co-catalyst. This study has triggered intensive research efforts on g-C_3N_4 for solar-fuel conversion.[126, 128] Nevertheless, the photocatalytic activity of as-synthesized g-C_3N_4 is substantially low, which is attributed to insufficient sunlight absorption, inefficient carrier separation, and fast recombination of charge carriers.[126, 129] Therefore, a number of strategies have been developed, including nanostructure design in the form of porous structures,[130, 131] nanospheres,[132, 133] helical nanostructures,[134] 1D nanostructures (nanorods, nanowires, nanobelts, and nanotubes),[135] bandgap engineering through structural-distortion,[136] non-metal doping (i.e. S, F, B, P),[137, 138] metal-doping (i.e. Pt, Pd, Fe, Zn, Cu),[139, 140] molecular doping/copolymerization (dicyandiamide-barbituric acid, dicyandiamide–2-aminobenzonitrile, dicyandiamide-diami-nomaleonitrile, dicyandiamide-3-aminothiophene-2-carbonitrile, and urea-phenylurea),[141, 142] dye-sensitization,[143] and construction of various semiconductor-semiconductor heterojunction[126, 129, 144] etc. In order to promote charge carrier separation and migration for enhanced

photocatalytic activity, g-C_3N_4 has been hybridized with various nanocarbon composites (i.e. highly conductive graphene, multi-walled carbon nanotubes, or reduced graphene oxide),[129, 145, 146] and with polymers to form all-polymeric nanocomposites. Additionally, incorporation of noble metal cocatalysts (i.e. Pt, Au, Ag) on g-C_3N_4 photocatalyst is found to accelerate charge separation and reduce the overpotential required for water redox reaction.[126] As noble metals are rare and expensive, a number of non-noble-metal cocatalysts have also been developed, such as $Ni(OH)_2$, NiS, NiS_2, MoS_2, $CoSe_2$ etc.[144, 147-149] It should be noted that depending on the precursor used for the synthesis of g-C_3N_4, the photocatalytic performance is found to be different due to the structural variations of the as-synthesized material.[126] Martin *et al.* reported a highly efficient g-C_3N_4 photocatalyst synthesized from a low cost precursor, urea, which exhibited an excellent hydrogen evolution rate of nearly 20 mmol h^{-1} g^{-1} in hydrogen half reaction under full arc irradiation with a QE of 26.5% at 400 nm.[150] The reported QE was claimed to be one order of magnitude higher than any existing g-C_3N_4 photocatalysts.[141, 151-153] The excellent activity of urea-derived g-C_3N_4 was attributed to the more negative conduction band edge position, and improved exciton distribution over its structure.

Very recently, Wang and co-workers reported another metal-free and visible light sensitive two-dimensional (2D) nitride photocatalyst. By carbon doping in hexagonal boron nitride (*h*-BN), ternary alloy boron carbon nitride (BCN) with band gaps of 2.08, 2.56, and 2.72 eV were synthesized using pyrolysis method.[154] The band edge positions of BCN alloys were found to straddle the redox potential of water, and the bandgap can be tuned by controlling the amount of carbon doping. The as-synthesized BCN alloy was shown to drive HER without any noble co-catalysts. However, Ni-Co layered double hydroxides (Ni-Co LDHs) were used as co-catalysts to promote O_2 evolution. The demonstration of visible light sensitive 2D metal-free nitrides i.e., C_3N_4 and BCN will stimulate further research on other earth abundant and stable 2D material family for photocatalysis.

Enhanced efficiency by engineering the near-surface band structure

The near-surface band structure plays a critical role in enhancing the efficiency and stability of the photocatalysts. In the case of nanostructured photocatalysts, the charge carrier extraction at the semiconductor-liquid interface is no longer diffusion limited, as the diffusion lengths of the photoexcited carriers are often larger than the physical dimension of the photocatalysts.[73] It has been reported by Kibria *et al.* that one of the major obstacles for achieving high efficiency and stable overall water splitting over the emerging nanostructured photocatalysts is directly related to the near-surface band bending.[155] The presence of upward (or downward) band bending is commonly measured for *n* (or *p*-type) semiconductors.[156] Such near-surface band bending is required for efficient charge carrier separation in a PEC system, wherein oxidation and reduction reactions occur on different electrodes. However, in the case of photocatalytic water splitting, the presence of any surface band bending suppresses either electrons' (in case of *n*-type semiconductors) or holes' (in case of *p*-type semiconductors) diffusion towards the semiconductor-liquid interface. Therefore, the overall water splitting reaction is hampered. In an effort to enhance the efficiency and stability of metal-nitride nanowire photocatalysts, Kibria *et al.* demonstrated that with a controlled amount of Mg dopant incorporation during the epitaxial growth process, the near-surface band bending can be precisely tuned.[155] Figure 7a illustrates the estimated E_F-E_V from X-ray photoelectron spectroscopy valence band spectrum (shown in the inset). It is seen that, with increasing Mg dopant incorporation, E_F-E_V, i.e., the near-surface band bending approximately, can be tuned from 2.6 eV to 0.5 eV, and the near-surface region can be transformed from *n*-type to weakly *p*-type; providing a viable approach to control the charge properties and charge carrier transfer at the semiconductor-liquid interface. By tuning the band bending on the nonpolar $(10\bar{1}0)$ surfaces of GaN nanowires using *p*-type Mg doping, an absorbed photon conversion efficiency (APCE) of ~51% was achieved under UV light, which was nearly two orders of magnitude higher than undoped GaN, shown in Fig. 7b.[155] Stable and stoichiometric dissociation of neutral pH water was further demonstrated on *p*-type GaN nanowire arrays. In order to enhance the efficiency under visible light, *p*-type Mg doping was further optimized in InGaN nanowires, shown in Fig. 8.[34, 157] Subsequently, a double-

band *p*-GaN/*p*-InGaN nanowire heterostructure was developed, wherein the near-surface band bending was optimized for GaN and InGaN using *p*-type Mg doping. The APCE can reach ~69% under visible light (up to 475 nm), which is the highest value ever reported under visible light. Using a double-band *p*-GaN/*p*-$In_{0.2}Ga_{0.8}N$ nanowire heterostructure and Rh/Cr_2O_3 core/shell HER co-catalyst loading, an STH efficiency of ~1.8% was demonstrated under concentrated sunlight (26 suns).[34] Ultrafast exciton and charge-carrier dynamics studies on such *p*-GaN/*p*-$In_{0.2}Ga_{0.8}N$ nanowires further revealed that the Rh/Cr_2O_3 core/shell HER co-catalysts significantly accelerated the carrier extraction at the nanowire-co-catalyst interface.[158]

Table 2: Photoelectrochemical water splitting using metal/nonmetal-nitrides listed in chronological order.

Photoelectrode	Co-catalyst	Light intensity (mW cm^{-2})	Electrolyte	Photocurrent (mA cm^{-2})	Efficiency	Ref. (year)
n^+-p-Si/n-GaN/TJ/ p-InGaN	Pt	130, AM 1.5G	1 M HBr	-40.6 at 0.26 V_{NHE}	ABPE=8.7% at 0.33 V_{NHE}	197 (2015)
InN/InGaN QD		100, Xenon lamp	pH 3 H_2SO_4 and 0.5 M Na_2SO_4	12.7 at 0 $V_{Ag/AgCl}$	IPCE=56% at 600 nm at 0 $V_{Ag/AgCl}$	184 (2015)
Coaxial InGaN/GaN MQW nanowire		150, AM 1.5G	1 M HCl	2.1 at 1 $V_{Cathode}$	ABPE=0.3%, at 0.4 $V_{Cathode}$, IPCE=15% at 350 nm at 1 $V_{Cathode}$	181 (2015)
u-GaN/AlN/n-GaN photocathode		110, 220, 330	0.5 M H_2SO_4	-2.0 (330 mW/cm^2) at -0.5 $V_{Ag/AgCl/NaCl}$		166 (2014)
InGaN/GaN MQW		100	1 M HBr	1.2 at V_{CE}=0	STH=1.5% at 0 V_{CE}	196 (2014)
InGaN/GaN nanoporous		100	1 M HCl	0.4 at V_{CE}=1.0	IPCE=46% at 355 nm	177 (2014)
InGaN nanowall		75	0.5 M HBr (pH 3)	3.4 at 0 $V_{Ag/AgCl}$	IPCE=16% at 350 nm	176 (2014)
n-InGaN planar photoanode		2000	1 M HCl, 1 M NaCl		Max Photo-conversion efficiency 0.23%	195 (2013)
Ta_3N_5 nanorod	Co_3O_4/CO $(OH)_2$	100, AM 1.5G	1 M NaOH	3.64 at 1.23 V_{RHE}	IPCE=39.5% at 400 nm and 1.23 V_{RHE}	192 (2013)
InGaN planar photoanode		500 W, Xe lamp	1M HBr, 0.5M H_2SO_4 1M HCl	2 at 1 V_{RHE}	IPCE=58% at 1.0 V_{RHE} 400-430 nm (H_2SO_4)	175 (2013)
InGaN nanowire	Pt	40	0.5 M H_2SO_4	5, -0.5 V_{NHE}	IPCE=40% at -0.45 V_{NHE} 400-430 nm (H_2SO_4)	182 (2013)
InGaN/GaN nanorod	NiO	100, AM1.5	1M NaOH	0.3, 1 V_{CE}		183 (2013)
InGaN/GaN core/shell nanowire		300 W Xe, AM1.5G	1 M HBr	23 at 1.0 $V_{Ag/AgCl}$	IPCE=27.6% at 350 nm and 1.0 $V_{Ag/AgCl}$	70 (2013)
GaN nanorod		100	0.5M HCl	5.5 at V_{CE}=1.0 V	0.26%	167 (2013)
GaN nanowire		13.2 at 350 nm	1 M HBr, 1 M KBr	14 (HBr) at 0.0 $V_{Ag/AgCl}$	IPCE=18% at 350 nm and 0.3 $V_{Ag/AgCl}$	168 (2013)
Ta_3N_5 films	Co $(OH)_x$	100, AM 1.5G	1 M NaOH	5.5 at 1.23 V_{RHE}	IPCE = 50% at 400-470 nm and 1.2 V_{RHE}	190 (2013)
Ta_3N_5 nanorod arrays	Co-Pi	100, AM 1.5G	0.5 M Na_2SO_4 (pH 13)	3.8 at 1.23 V_{RHE}	IPCE = 41.3% at 440 nm	193 (2013)
Ta_3N_5 films	Co_3O_4	100, AM 1.5G	1 M NaOH	3.1 at 1.2 V_{RHE}	IPCE = 36–40% at 400-500 nm and 1.2 V_{RHE}	194 (2012)

Table 2 (*Contd.*)

Photoelectrode	Co-catalyst	Light intensity (mW cm^{-2})	Electrolyte	Photocurrent (mA cm^{-2})	Efficiency	Ref. (year)
Si/InGaN core/shell nanowire		350 without AM 1.5	pH 3 H_2SO_4 with 0.5 M of Na_2SO_4	62.6 μA/cm^2 at V_{RHE}=1.23		178 (2012)
Ta_3N_5 nanotube	IrO_2, Co_3O_4, Pt, Co-Pi	110	0.1 M Na_2SO_4	-1.2 (IrO_2), -1.0 (Co_3O_4), -0.8 (Co-Pi), -0.25 (Pt),	IPCE 10% 0.6 $V_{Ag/AgCl}$ for Ta_3N_5 /IrO_2	188 (2012)
InGaN film		500 W Xe lamp	1 M HBr	0.5 at 0.8 V vs Ag/AgCl	IPCE=42% at 400 nm 0.8 V vs Ag/AgCl	114 (2011)
Ta_3N_5	IrO_2		0.1 M Na_2SO_4 (pH 6)	3.8 at 1.15 V_{RHE}	IPCE=31% at 500 nm and 1.15 V_{RHE}	189 (2011)
p-InGaN		132	1 M HBr	1.2, at V_{CE}=1.2 V		173 (2010)
Ta_3N_5 nanotube			1 M KOH		IPCE 5.3% 0.5 V_{CE} at 450 nm	187 (2010)
W_2N nanowire		100, AM1.5	0.5 M, H_2SO_4	1.5 at V_{SCE}=1.2	ABPE=0.4% at 0.84 V_{SCE}	186 (2009)
InGaN film		500 W Xe lamp	1 M HCl	25 at V_{CE}=1.0 V		172 (2008)
InGaN film		500 W Xe lamp	1 M HBr	1.0 at V_{SCE}=0.8	IPCE=9% at 400-430 nm at V_{SCE}=0.8	174 (2008)
GaN patterned		4200	1 M NaOH	17.34 at 0.50 V_{CE}	ABPE=0.3% at 0.50 V_{CE}	161 (2007)
GaN patterned		110	1 M HCl	0.48 at 0 V_{CE}	STH=0.61% at 0.0 V_{CE}	159 (2007)

Photoelectrochemical water splitting using metal/nonmetal-nitride photoelectrodes

Recently, photoelectrochemical water splitting using metal/nonmetal-nitrides has also gained considerable attention. Planer and nanostructured GaN has been employed as UV light active photoelectrodes. For visible light activity, InGaN and Ta_3N_5 have been commonly studied.

UV light responsive metal/nonmetal-nitride photoelectrodes

Fujii *et al.* observed H_2 gas generation using an *n*-type GaN photoelectrode at 1.0 V_{CE} in 2005.[76] While n-GaN was found to be stable in HCl, photocorrosion was observed in KOH electrolyte.[78] Fujii *et al.* also reported that the band-edge potentials of *p*-GaN were identical to that of *n*-GaN.[77] The incorporation of a suitable dopant in GaN photoelectrode is one of the strategies to enhance the device efficiency. M. Ono *et al.*

reported carrier concentration dependent PEC properties of *n*-GaN photoanode.[159] The maximum photocurrent was measured with a carrier concentration of 1.7×10^{17} cm^{-3}. Fujii *et al.* reported that the presence of alcohol in the NaOH electrolyte increased the H_2 evolution rate nearly twice compared to that without alcohol.[160] The higher H_2 production activity in the presence of alcohol was attributed to easier oxidation of alcohol compared to that of water. The existence of alcohol further suppressed photocorrosion of GaN caused by self-oxidation. By patterning a planar *n*-type GaN surface with metal stripes and *n*-GaN ridges, Waki *et al.* achieved higher photocurrent density in 1M NaOH.[161] This higher photocurrent was attributed to the eradication of current crowding effect and the enhancement in effective surface area for photoelectrolysis. Current crowding effect can also be minimized by placing immersed finger-type indium tin oxide (IF-ITO) ohmic contacts on *n*- and *p*-GaN photoelectrode to achieve enhanced photocurrent and H_2 generation rate.[162, 163] Kikawa *et al.* measured flat-band potentials of Ga-face and N-face *n*-GaN, and found that the conduction band edge of N-face was ~0.3 eV more negative than that of Ga-face GaN.[164] As a consequence, more hydrogen bubbles and cathodic current were observed on N-face than that of Ga-face GaN. In contrast, from Mott-Schottky analysis, Lin *et al.* concluded that the conduction band edge of Ga-polar GaN was ~0.4 eV more negative than that of N-polar GaN.[165] While Ga-polar surface was found to have higher photoconversion efficiency at negative bias (vs. Pt counter electrode), N-polar surface exhibited higher photoconversion efficiency at positive bias (vs. Pt counter electrode). By utilizing the spontaneous and piezoelectric polarization in Wurtzite III-nitrides, Nakamura *et al.* demonstrated a polarization-engineered GaN/AlN/GaN photocathode without *p*-type doping.[166] This novel photocathode showed enhanced cathodic photocurrent compared to *p*-GaN in H_2SO_4 electrolyte.

Nanostructuring the photoelectrode can lead to enhanced light absorption, suppressed carrier recombination, and efficient carrier extraction. Up to 6 times enhancement in photocurrent density was demonstrated with GaN nanorod arrays compared to GaN planar photoelectrode.[167] The H_2 evolution rate increased from 0.1 to 0.73 ml h^{-1} cm^{-2} and STH conversion efficiency increased from 0.04% to 0.26% using the nanorod arrays. The PEC properties of PAMBE grown undoped and Si-doped GaN nanowire arrays were

studied in HBr and KBr electrolyte by AlOtaibi *et al.*[168] Maximum IPCE values of ~15% and ~18% were measured for undoped and Si-doped GaN nanowires at -0.1 and 0.3 V vs. Ag/AgCl under 350 nm excitation, respectively. It was further demonstrated that the electrochemical properties of GaN nanowires can be tuned with controlled doping and external bias via the electrolyte.[169]

Visible light responsive metal/nonmetal-nitride photoelectrodes

A number of strategies have been developed to enhance the light absorption of nitrides in the visible spectral range. Liu *et al.* demonstrated visible light (400 – 600 nm) activity of Mn-doped GaN photoelectrode with an IQE of 61% at 450 nm.[170] This visible light response was attributed to Mn-related intermediate band formed in the bandgap of GaN. However, photocorrosion of the electrode was inevitable owing to the presence of Mn-related structural defects in GaN.

Fujii *et al.* studied PEC properties of InGaN for H_2 generation in 2005.[171] At 1 V_{CE}, the $In_{0.02}Ga_{0.98}N$ photoelectrode showed higher photoactivities compared to GaN photoelectrodes in 1M HCl. Later on, Li *et al.* studied the PEC properties of 200 nm thick *n*-InGaN epilayer grown by MOCVD.[172] A drastic enhancement in photocurrent density and hydrogen evolution rate was demonstrated by increasing the In content from 20 to 40%. Aryal *et al.* reported excellent stability of *p*-$In_xGa_{1-x}N$ ($0 \leq x \leq 0.22$) epilayer in aqueous HBr solution.[173] In another study, Luo *et al.* demonstrated good photostability and visible light response from MOCVD grown 60 nm thick $In_{0.2}Ga_{0.8}N$ electrode in aqueous HBr solution.[174] The turnover number reached 847 after 4000 s irradiation, and the incident photon conversion efficiency (IPCE) was nearly 9% under 400–430 nm at 0.8 V vs. SCE. In a subsequent report, in order to enhance the IPCE, the authors grew 250 nm thick $In_{0.2}Ga_{0.8}N$. However, the In-rich InGaN phases caused by In segregation on the surface reduced the photocurrent owing to the presence of surface recombination centers.[114] By removing this In-rich InGaN phases using 1M HCl aqueous solution, the IPEC was found to increase from 15% to 42% at 400 nm at 0.8 V vs. Ag/AgCl with enhanced stability of the photocurrent. The authors further demonstrated an IPCE of 53%

and 58% under 400-430 nm at 1 V vs. RHE after surface treatment of $In_{0.3}Ga_{0.7}N$ in HBr and H_2SO_4 aqueous solution, respectively.[175]

A number of metal-nitride nanostructured photoelectrodes have been developed for efficient water splitting. Nearly 57% enhancement in H_2 evolution rate was revealed in the case of PAMBE grown In rich (40-50%) InGaN nanowall structures compared to that of planar InGaN.[176] Benton *et al.* fabricated nanoporous structures of GaN and InGaN/GaN by photoelectrochemical etching in KOH solution.[177] An IPCE of 32% and 46% at 355 nm was demonstrated for GaN and InGaN/GaN nanoporous structures, respectively, which were nearly 4-fold higher than as-grown planer devices. In order to enhance the effective surface area, Si/InGaN core/shell hierarchical nanowire were synthesized using photolithography and CVD to function as a photoanode for water splitting.[178] Nearly 5 times enhancement in photocurrent density was demonstrated for hierarchical $Si/In_xGa_{1-x}N$ (x=0.08-0.1) nanowires compared to that of InGaN nanowires on planar Si substrate reported by the same group. However, the photocurrent recorded from $Si/In_xGa_{1-x}N$ (x=0.08-0.1) nanowire electrode was very small (~10 $\mu A/cm^2$ at 1 V_{RHE} under 1 sun), which was attributed to fast carrier recombination and inefficient charge transfer at the semiconductor/electrolyte interface. On the other hand, AlOtaibi *et al.* reported *n*-type $In_{0.3}Ga_{0.7}N$/GaN core/shell double-band nanowire photoanode grown by PAMBE on Si (111) substrate, illustrated in Fig. 9.[70] The core/shell double-band nanostructures provided efficient light absorption and stable photoelectrochemical reaction in HBr electrolyte. Stable PEC water splitting and H_2 generation under UV and visible light (up to 600 nm) were demonstrated with an IPCE of 27.6% under 350 nm excitation at 1 V vs. Ag/AgCl. Caccamo *et al.* compared the photocurrent density of single crystalline *n*-type GaN/$In_{0.3}Ga_{0.7}N$ (core/shell) nanorods with that of GaN nanorods synthesized by selective area growth metal organic vapour phase epitaxy (MOVPE).[179] While the photocurrent was the same for both electrodes for applied potential up to 1 V vs. RHE, nearly 10-fold higher photocurrent density was observed in the case of GaN/$In_{0.3}Ga_{0.7}N$ (core/shell) nanorods at 1.35 V vs. RHE. Ebaid *et al*. recently synthesized coaxial InGaN/GaN multiple quantum well (MQW) nanowire heterostructure photoanodes using MOCVD.[180] With careful optimization of the In content and number of QWs, such MQW nanowire

heterostructure enabled stable water splitting in 1M HCl with maximum IPCE of 8.6% at 350 nm at 1 $V_{cathode}$ and applied bias photon-to-current efficiency (ABPE) of 0.21% at 0.4 $V_{cathode}$. The same group further studied the carrier dynamics on InGaN/GaN MQW coaxial nanowires to improve the efficiency.[181] Defect-induced recombination and strong localization of excitons were revealed in samples with thin QWs (up to 3 nm). In contrast, strong band-to-band transitions and negligible localization were observed in samples with thick QWs (~6 nm). By carefully engineering the InGaN QW thickness to reduce the carrier localization and defect density in coaxial nanowires, an IPCE of 15% at 350 nm at 1 $V_{cathode}$ was achieved.

The PEC properties of *n*- and *p*-type InGaN nanowires grown by PAMBE for water splitting were studied by *in situ* electrochemical mass spectroscopy (EMS) in 0.5M H_2SO_4.[182] An IPCE of 40% at a potential of -0.5 V vs. NHE was measured in the visible spectrum. Stable photocurrent and H_2 evolution was observed for 60 mins. The PEC properties of InGaN/GaN nanorod LED structure grown by MOCVD was studied by Benton *et al.*[183] The photochemical etching of the nanowires owing to self-oxidation by the photogenerated holes in aqueous NaOH solution was significantly suppressed by incorporating NiO nanoparticles onto the nanowires. The NiO nanoparticles help to suppress carrier recombination and promote oxidation reaction on its surfaces rather than on the nanowire surface. Alvi *et al*. recently demonstrated that PAMBE grown InN quantum dot decoration doubled the PEC efficiency of $In_{0.54}Ga_{0.46}N$ photoelectrodes, with a maximum IPCE of up to 56% at 600 nm at 0 V vs. Ag/AgCl and stable photocurrent for over 10 hrs.[184] Rajaambal *et al.* reported InGaN QDs on ZnO for efficient visible light absorption with high photostability for solar light harvesting.[185]

Apart from group-III metal-nitrides, a few other metal-nitride photoelectrode materials have also been reported. Chakrapani *et al.* studied PEC properties of tungsten nitride (W_2N) nanowire arrays.[186] While W_2N showed *n*-type behavior with good photoactivity at moderate bias, prolonged photolysis resulted in photocorrosion of the nanowires due to the presence of defects. However, mixed phase W_2N-WO_3 showed improved photo-stability. Feng *et al.* synthesized highly oriented Ta_3N_5 nanotube arrays for visible light responsive photoelectrolysis.[187] In a two-electrode arrangement, an IPCE of 5.3% was achieved at 450 nm

with 0.5 V_{CE} bias in KOH solution. Cong *et al.* studied the PEC water oxidation properties of Ta_3N_5 nanotubes decorated with IrO_2, Co_3O_4, Co-Pi, and Pt nanoparticles under visible light.[188] The Ta_3N_5 nanotube showed three times higher photocurrent than regular Ta_3N_5 film. The PEC water oxidation on Ta_3N_5 nanotube was improved by IrO_2, Co_3O_4, and Co-Pi nanoparticles. A maximum IPCE of ~10% at 400 nm was demonstrated for IrO_2 decorated Ta_3N_5 nanotube arrays at 0.6 $V_{Ag/AgCl}$. Higashi *et al.* demonstrated an efficient Ta_3N_5 photoanode for overall water splitting into H_2 and O_2 under visible light. By performing a necking treatment ($TaCl_5$ treatment + NH_3 treatment) and loading $IrO_2.nH_2O$ OER co-catalyst nanoparticles on Ta_3N_5 photoanode, an IPCE of 31% at 500 nm with 1.15 V vs. RHE in aqueous Na_2SO_4 solution was demonstrated.[189] Li *et al.* reported that by thermal or mechanical exfoliation of surface recombination centers and loading $Co(OH)_x$ OER co-catalysts, the IPCE of Ta_3N_5 photoanodes can be significantly improved.[190] A highest photocurrent (among all currently available Ta_3N_5 photoanodes to our knowledge) of 5.5 mA cm^{-2}, which corresponds to an IPCE of 50% under 400-470 nm at 1.23 V vs. RHE in aqueous NaOH solution was demonstrated.[189-194] However, the photocurrent was reduced to 55% in 2h of illumination, which is attributed to oxidation of Ta_3N_5 by the photogenerated holes. To address the poor photostability of Ta_3N_5 for water oxidation, Liu *et al* reported a ferrihydrite (Fh) passivation layer that allows stable water oxidation for over 6 h with a benchmark photocurrent over 5.2 mA cm^{-2} at 1.23 V vs. RHE.[191] The remarkably enhanced photostability of Fh/Ta_3N_5 is attributed to the hole storage capability of Fh layer.

In an effort to reduce the required external bias for PEC water splitting, photovoltaic devices have been integrated with nitride photoelectrodes for efficient solar energy conversion. An *n*-InGaN working electrode has been developed which is biased by a GaAs solar cell.[195] By optimizing the electrolyte and incident light intensity, and introducing immersed ITO ohmic contacts on the *n*-InGaN working electrode, the operating point of the device was tuned to match the maximum power point of the GaAs solar cell. A photoconversion efficiency of 0.18-0.23% was demonstrated under simulated sunlight with optimized conditions. In another study, Dahal *et al.* realized a monolithic solar-PEC device based on InGaN/GaN MQW solar cell.[196] An STH efficiency of 1.5% was reported at zero bias (V_{CE}=0 V). Excellent chemical stability was further

demonstrated for a prolonged period of time (7 days) in aqueous HBr solution. Fan *et al.* recently synthesized dual absorber photocathode, consisting of *p*-InGaN/tunnel junction/n-GaN nanowire arrays on a Si solar cell wafer using PAMBE, illustrated in Fig. 10.[197] Such monolithically integrated dual absorber nanowire photocathode can operate efficiently without strict current matching between different absorbers, which is required for conventional planar tandem photoelectrodes. Unlike planar tandem photoelectrode, wherein carrier extraction is possible only from the front surface, the one-dimensional nanowire architecture allows for lateral carrier extraction from different absorber layers for efficient redox reactions. Additionally, the insertion of n^{++}-GaN/InGaN/p^{++}-GaN polarization-enhanced tunnel junction (shown in Fig. 11a) allows for efficient carrier transport along the axial direction of the nanowires. While platinized n^{+}-p Si solar cell wafer produced a photocurrent of -20 mA/cm^2 at 0 V_{NHE}, the platinized *p*-InGaN/tunnel junction/*n*-GaN nanowire on n^{+}-p Si solar cell wafer generated a photocurrent of -40 mA/cm^2 at 0 V_{NHE}. The Pt nanoparticle decorated monolithically integrated photocathode exhibited an ABPE of 8.7% at 0.33 V_{NHE} and nearly unity Faradic efficiency for H_2 generation. The InGaN/GaN photocathode also exhibited stable photoactivity over 3hrs. Very recently, AlOtaibi *et al.* demonstrated III-nitride nanowire based dual-photoelectrode device to enhance the efficiency of conventional 2-photon tandem devices under parallel illumination by splitting the solar spectrum spatially and spectrally,[198] illustrated in Fig. 11. The dual-photoelectrode, consisting of a GaN nanowire photoanode and an InGaN nanowire photocathode, exhibited an open circuit potential of 1.3 V and nearly 20-fold enhancement in the power conversion efficiency under parallel illumination (400-600 nm), compared to that of individual photoelectrodes. Furthermore, a dual-photoelectrode, consisting of parallel-connected metal-nitride nanowire photoanodes and a monolithically integrated single-junction-Si/InGaN nanowire photocathode, exhibited an ABPE of 2% at ~ 0.6 V vs. the photocathode, illustrated in Fig. 11c.

Photocatalytic and photoelectrochemical CO_2 reduction using metal/nonmetal-nitrides

To date research efforts on artificial photosynthesis are mostly directed towards sunlight-driven water splitting to produce H_2 fuel. Although H_2 is an important fuel and chemical feedstock, it suffers from low volumetric energy densities[3]. In contrast, hydrocarbon fuels with optimum volumetric energy density can be

a practical alternative for better integration with existing energy infrastructure. Therefore, photocatalytic and photoelectrochemical CO_2 reduction to high-energy-rich fuels is of tremendous interest. This process not only produces value-added fuels from abundant natural resources, but also provides an alternative approach to capture, sequestrate, and store anthropogenic CO_2. For photocatalytic CO_2 reduction, the bandgap of the semiconductor needs to straddle the oxidation potential of water and reduction potential of CO_2 to various hydrocarbons. Upon bandgap irradiation, photoholes in the valence band of a semiconductor oxidize water to generate O_2 and H^+, and photogenerated electrons in the conduction band reduce CO_2 by a sequence of reactions to produce CO, CH_4 or CH_3OH etc.[16]

Since the first demonstration of photoelectrochemical and photocatalytic CO_2 reduction to hydrocarbons (HOOCH, CH_2O, CH_3OH, CH_4) by Halmann[20] in 1978 and Inoue[21] in 1979, respectively, many groups have investigated the use of different semiconductors to achieve enhanced catalytic activities.[16] Although a number of UV light sensitive photocatalysts (e.g., GaN, ZnS, SiC, $SrTiO_3$, and TiO_2) have been found that are catalytically active, the development of visible light sensitive photocatalyts is still very limited.[15] Illustrated in Fig. 2, in contrast to most of the commonly used metal-oxides, the bandgaps of nitrides straddle the oxidation potential of water and reduction potential of CO_2. Therefore, the development of various metal/nonmetal-nitride based photocatalysts for CO_2 reduction has attracted significant attention recently.

AlOtaibi *et al.* has recently demonstrated photocatalytic CO_2 reduction to CH_4 and CO using GaN nanowire arrays with light being the only energy input.[199] While the bare GaN nanowire was found to have higher photoactivity for CO production over CH_4, the Rh/Cr_2O_3 core/shell nanoparticle decorated GaN nanowires provided higher activity and selectivity towards CH_4 over CO production. Additionally, Pt nanoparticle decorated GaN nanowires showed an order of magnitude higher photoactivity for CH_4 production than bare GaN nanowires, with over 24 hrs of stability. Yotsuhashi *et al.* demonstrated that *n*-type Si doped GaN epilayer photoanode grown by MOCVD could produce HCOOH with 3% Faradic efficiency with light being the only energy input.[200] Later on the Faradic efficiency of GaN epilayer was improved to 9%

by enhancing the water oxidation of GaN with NiO co-catalysts.[201] In a follow-up study, the efficiency of the photoanode was improved by using AlGaN/GaN heterostructures.[202, 203] In a subsequent study, a tandem photoanode of InGaN with two Si p-n junctions was developed for CO_2 reduction to HCOOH with an energy conversion efficiency of 0.97%.[204] While InGaN enhanced the light absorption of the photoanode, the embedded Si p-n junction raised the cathode potential for CO_2 reduction and enhanced the reaction capability of the cathode.

Since the first demonstration in 2009, polymeric C_3N_4 has been widely studied as a visible light sensitive catalyst for CO_2 reduction.[126, 205-211] It has been demonstrated that the CO_2 photoreduction activity and selectivity of the products is highly dependent on the structure of the g-C_3N_4 and the co-catalysts used. For example, melamine hydrochloride precursor derived g-C_3N_4 effectively photocatalyze CO_2 reduction into CO under visible light without any co-catalyst.[212] In another study, urea derived g-C_3N_4 was found to be more effective than melamine-derived g-C_3N_4 due to improved reaction surface area, and small crystal size.[209] The incorporation of Pt co-catalyst on g-C_3N_4 was reported to enhance photocatalytic activity and selectivity for CO_2 reduction into CH_3OH, CH_4, HCHO etc.[213] Bai *et al.* reported that the Pd{111} facets of Pd co-catalyst were more active than Pd{100} facets for CO_2 photoreduction.[214] Lin *et al.* demonstrated an inexpensive system consisting of g-C_3N_4 photocatalyst, CoO_x oxidative co-catalyst, and Co-bipyridine complex ($Co(bpy)_3^{2+}$) electron mediator, that can reduce CO_2 to CO under visible light.[206] Heterojunctions of g-C_3N_4/In_2O_3,[215] and g-C_3N_4/red-phosphor[216] were also found to be effective for CO_2 photoreduction to CH_4 under visible light. Maeda and co-workers demonstrated that molecular ruthenium complex coupled polymeric C_3N_4, shown in Fig. 12, can photocatalytically reduce CO_2 to HCOOH under visible light with a high turnover number (200 for 20 hrs) and high selectivity (80%).[208] A follow-up work on this hybrid photocatalyst revealed that the introduction of mesoporosity into C_3N_4 structures can increase the specific surface area and hence the activity.[207] In a subsequent work, by carefully designing the catalytically active site and the reaction environment, a substantial improvement in the photocatalytic conversion of CO_2 into formic acid was achieved, leading to a relatively high TON (>1000) and AQY of 5.7% at 400 nm.[205] Very

recently, 2D BCN has been developed, which can photocatalytically reduce CO_2 to CO under visible light (>420 nm).[154]

Conclusions and perspectives

In summary, we have provided an overview of the current research status of metal/nonmetal-nitride based photocatalysts and photoelectrodes for artificial photosynthesis. Over the last decade, metal/nonmetal-nitrides have emerged as a new generation of photocatalysts owing to their unique optoelectronic and photocatalytic properties. A number of nitride based photocatalysts and photoelectrodes have been developed in recent years that can function effectively for solar water splitting and CO_2 reduction under UV and visible light. Nearly 10 years of research efforts on nitrides has seen more success, to some extent, than what has been achieved from nearly 40 years of dedicated research on metal-oxide based materials for solar-fuel conversion.

While STH efficiency of a few percentages and a few hours of stability have been achieved to date, it is far from the target STH efficiency of >10% with long-term stability (5000 hrs) to meet the DOE's target cost of \$2-4/Kg H_2 by 2018.[217] Therefore, the synthesis of new materials and development of new technologies are needed. Although significant research efforts have been made to develop UV and visible light sensitive photocatalysts, little attention is paid to harness the infrared light, which constitutes about 52% of the solar spectrum. Synthesis of defect-free In rich InGaN (In~50-100%) photocatalysts could harness a large part of the solar spectrum. For near-infrared (up to 2,000 nm) light absorption, InN with a bandgap of 0.65 eV can be utilized. Since InN does not possess sufficient potential for HER, it can be utilized in combination with another small bandgap semiconductor with sufficient HER potential in a Z-scheme to capture ~80-90% of the solar spectrum. The tunable bandgap of InGaN enables the synthesis of a quadri-band photocatalyst, which can be one of the potential options for better utilization of the entire solar spectrum. Utilization of other potential technologies, such as multiple exciton generation[218], hot electron transfer, and up-conversion[219] may help overcome the efficiency bottleneck as well. Moreover, because of their earth-abundance, excellent photovoltaic properties, strong photon absorption, and large carrier diffusion lengths, perovskite based PV

(or their integration with Si based PV) may contribute to the long waited breakthrough in solar hydrogen race.[44, 220-222] However, the stability of perovskite material remains a major concern to achieve this goal. Apart from novel material development, the reaction kinetics, *i.e.,* detailed thermodynamics and kinetics in interfacial carrier transfer in water splitting and CO_2 reduction need to be further understood to improve the efficiency and stability of the existing photocatalyst materials. An optimum photocatalyst should possess enhanced light absorption, rapid carrier collection/extraction, and wider solar spectrum absorption, lowered cost and toxicity, and enhanced stability. Because of their tunable bandgap, unique optoelectronic and catalytic properties, it is expected that metal/nonmetal-nitrides will stimulate further research to overcome the efficiency and reliability bottleneck of metal-oxides, Si, and other commonly used photocatalysts for commercially viable artificial photosynthetic devices in the near future.

Acknowledgement

This work was supported by the Natural Sciences and Engineering Research Council of Canada (NSERC) and the Climate Change and Emissions Management (CCEMC) Corporation.

Figures

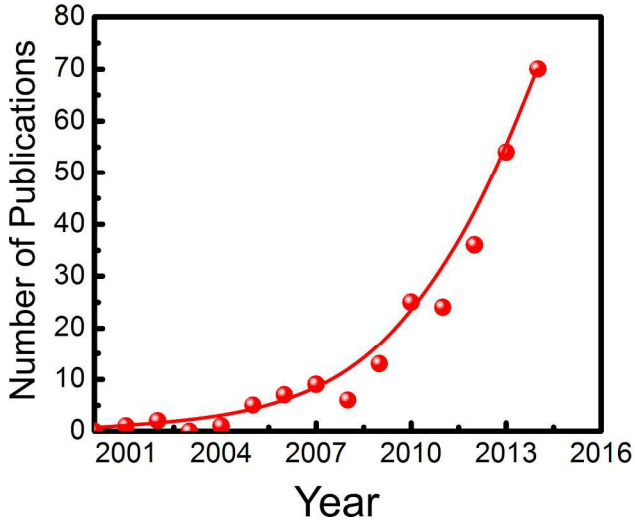

Figure 1: The rise of nitrides. Annual number of publications in Web of Science when a search for the topic "water splitting" and "nitride" was performed.

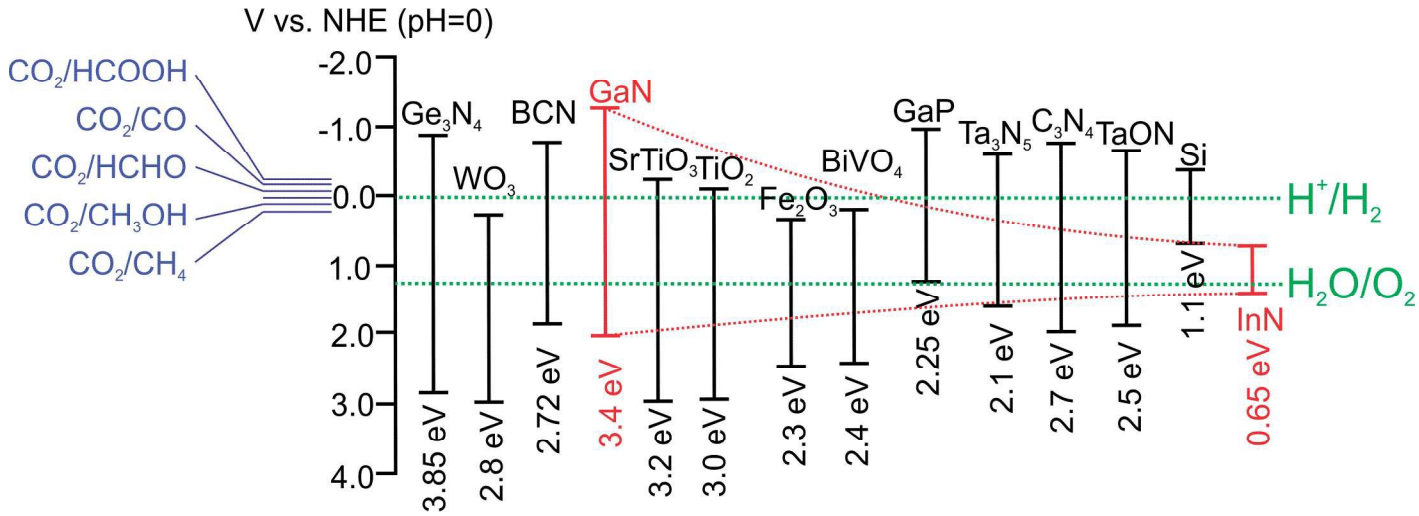

Figure 2: Band edge positions of commonly reported nitride photocatalysts. The oxidation and reduction potentials of water are also shown (green dotted lines). The red dotted line represents the band edge positions of $In_xGa_{1-x}N$ with x increasing from left to right (0-1). The reduction potentials of CO_2 to various value added products are also shown.

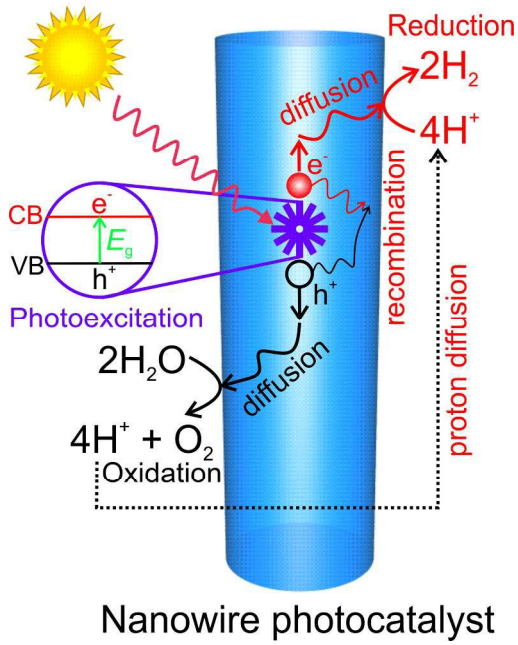

Figure 3: Schematic illustration of the main process steps in water splitting, including photoexcitation, carrier generation, diffusion, recombination, water oxidation, proton diffusion, and reduction reaction on the surface of nanowire photocatalysts.

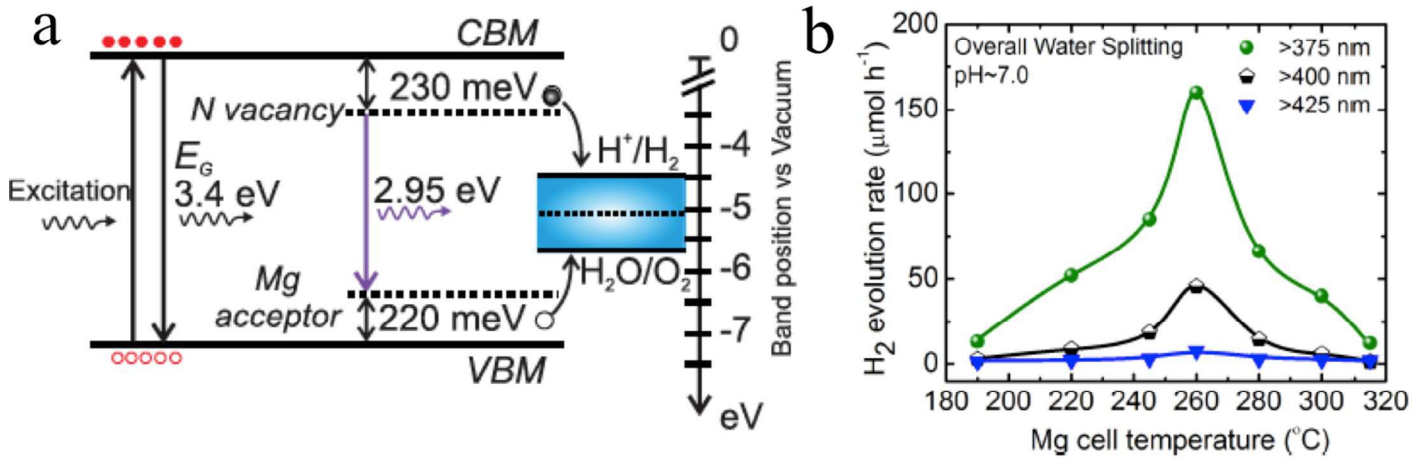

Figure 4: (a) Schematic energy band diagram of GaN:Mg nanowires illustrating the formation of nitrogen vacancy (V_N) and Mg acceptor related intra-gap states, along with the redox potential of water (vs. vacuum level). (b) H_2 evolution rate from overall neutral water splitting from different Mg doped GaN (GaN:Mg) samples with different intra-gap excitations using a 300 W Xenon lamp and long-pass optical filters.[110]

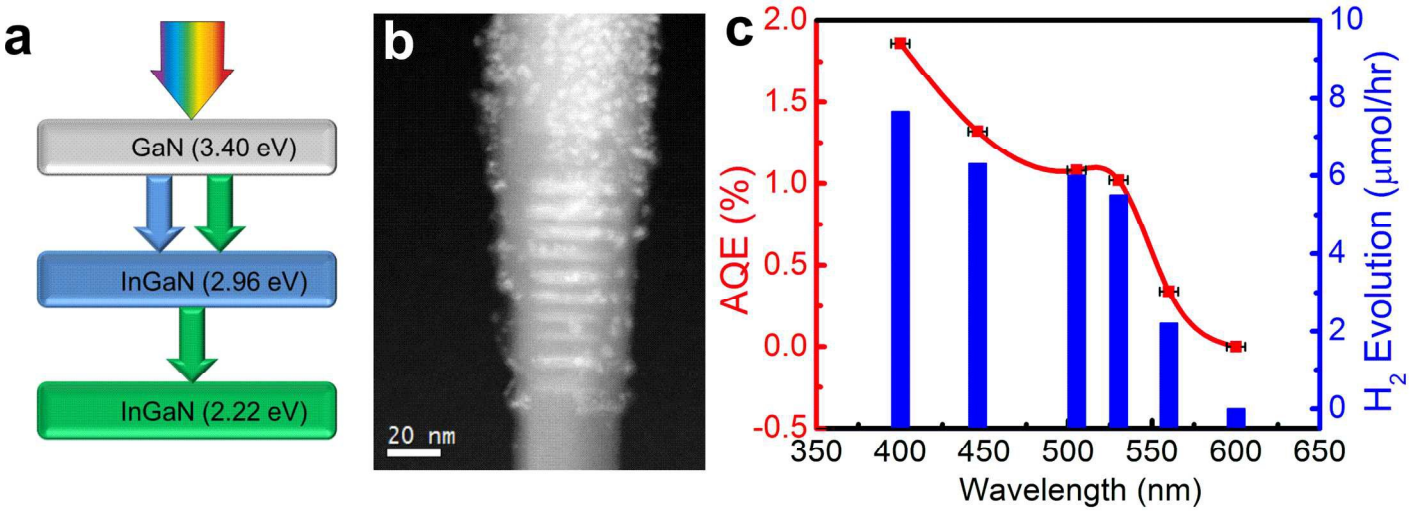

Figure 5: (a) Schematic of a triple-band InGaN/GaN nanowire heterostructure, illustrating the light absorption process. (b) Electron energy loss spectroscopy (EELS) spectrum image of Rh/Cr_2O_3 core/shell nanoparticle decorated triple-band InGaN/GaN nanowire heterostructure. (c) Apparent quantum efficiency (AQE) and rate of H_2 evolution vs. excitation wavelength. The experiment was performed in neutral pH water under 300 W Xenon lamp irradiation with different band-pass filters without any other energy input. The horizontal error bars represent the full-width-half-maximum of the bandpass filters. The red solid line is a guide to the eye.[118]

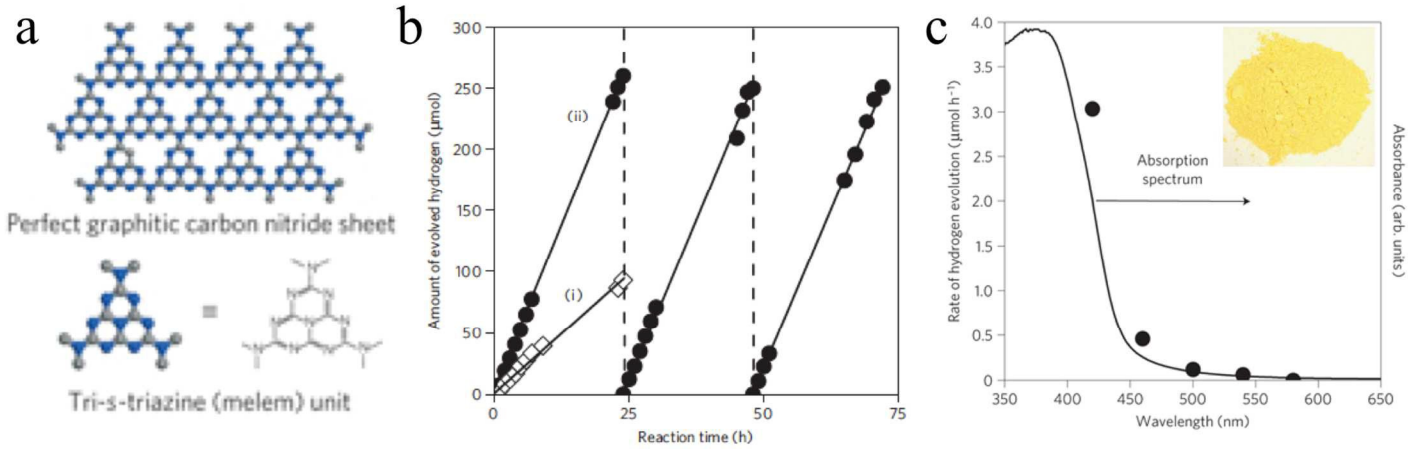

Figure 6: (a) Schematic illustration of perfect g-C_3N_4 sheet constructed from melem units. (b) H_2 production from water in the presence of sacrificial electron donor (10 vol% triethanolamine) under visible light (>420 nm) by (i) unmodified g-C_3N_4 and (ii) 3.0 wt% Pt-deposited g-C_3N_4 photocatalyst. (c) H_2 production rate from water in the presence of sacrificial electron donor (10 vol% methanol) by 0.5 wt% Pt-deposited g-C_3N_4 photocatalyst vs. wavelength of the incident light. UV–visible absorption spectrum of the g-C_3N_4 catalyst is also shown for comparison.[80]

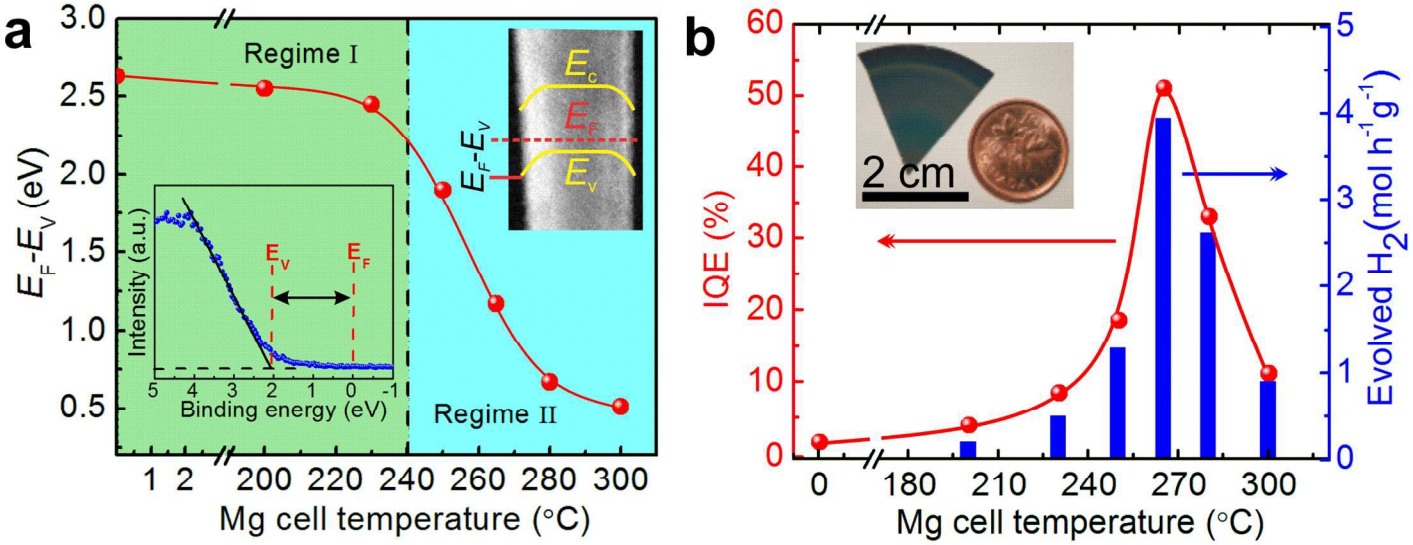

Figure 7: (a) Estimated E_F-E_V from angle resolved X-ray photoelectron spectroscopy valence spectrum (lower left inset) for different Mg doped GaN nanowire samples. The upper right inset shows the downward band bending and E_F-E_V on the TEM image of a single GaN nanowire. The dotted vertical line separates Regime I (*n*-type surface) from Regime II (*p*-type surface). (b) Internal quantum efficiency (IQE) and rate of H_2 evolution from overall neutral water splitting by ~0.387 mg GaN:Mg nanowire catalyst with different Mg doping concentrations under 300 W Xenon lamp irradiation. The Mg incorporation in GaN nanowires is directly proportional to the Mg cell temperature.[154]

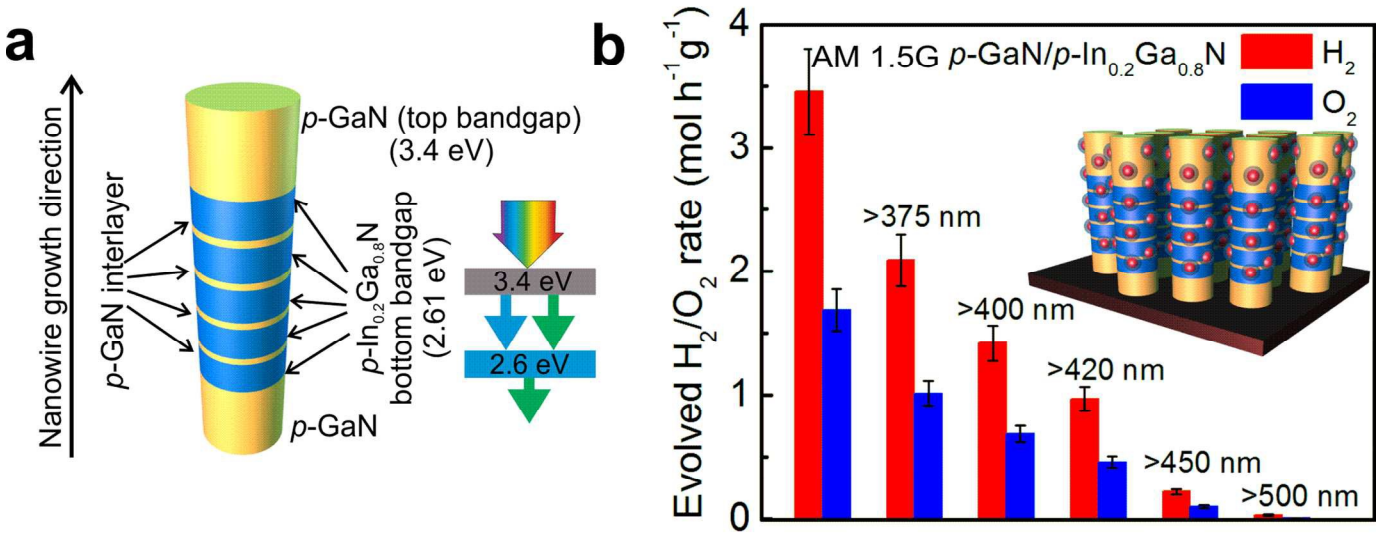

Figure 8: (a) Schematic of a double-band GaN/$In_{0.2}Ga_{0.8}N$ nanowire photocatalyst. Five *p*-InGaN nanowire segments are incorporated along the growth axis of *p*-GaN nanowire for visible light absorption. The inset shows the light absorption by the double-band structure. (b) Rate of H_2 and O_2 evolution from the Rh/Cr_2O_3 core/shell nanoparticle decorated double band GaN/InGaN nanowires. The reaction was performed using ~0.48 mg catalyst in neutral pH water under 300 W Xenon lamp irradiation with AM1.5 filter and various long-pass filters without any other energy input. The inset shows core/shell Rh/Cr_2O_3 nanoparticle decorated GaN/InGaN nanowires.[34]

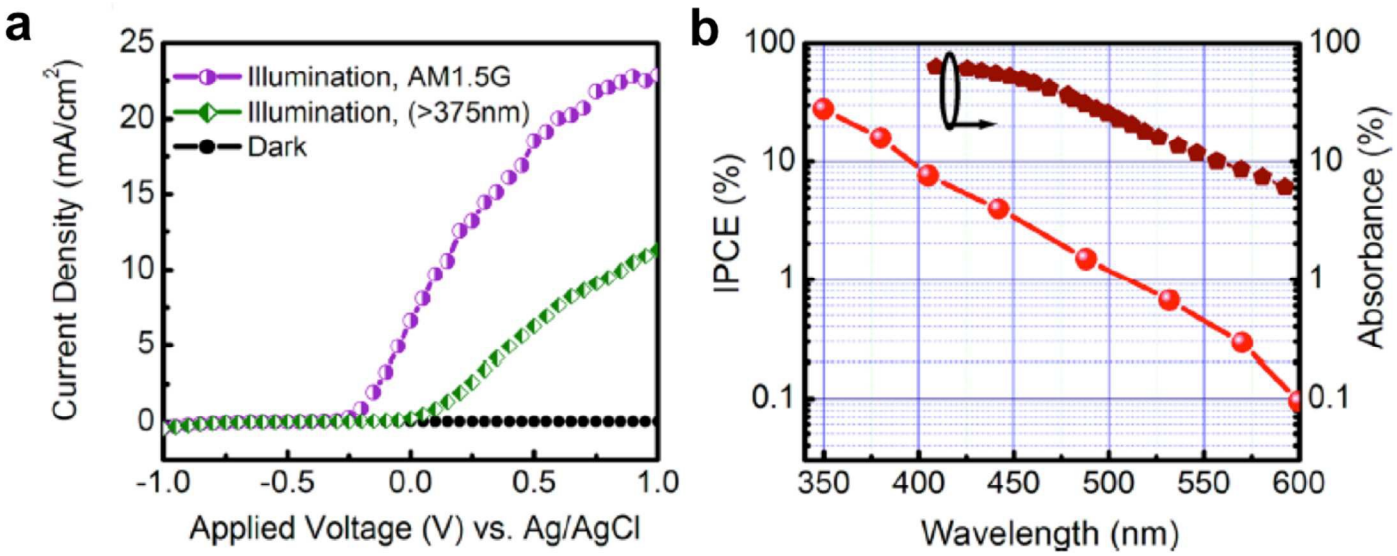

Figure 9: (a) Current density vs. applied voltage (vs. Ag/AgCl) in 1 M HBr under 300 W Xenon lamp irradiation. The visible light response from InGaN nanowires is confirmed by adopting a long-pass (>375 nm) filter. The measured current density is ~23 mA/cm^2 using a 300W Xe lamp with AM1.5G filter at a bias of 1 V (vs. Ag/AgCl). (b) Incident-photon-to-current conversion efficiency (IPCE) of InGaN/GaN nanowire photoelectrodes measured at 1 V (vs. Ag/AgCl) in 1 M HBr in a semi log scale. The calculated spectral absorbance by the InGaN segments is also shown for comparison.[70]

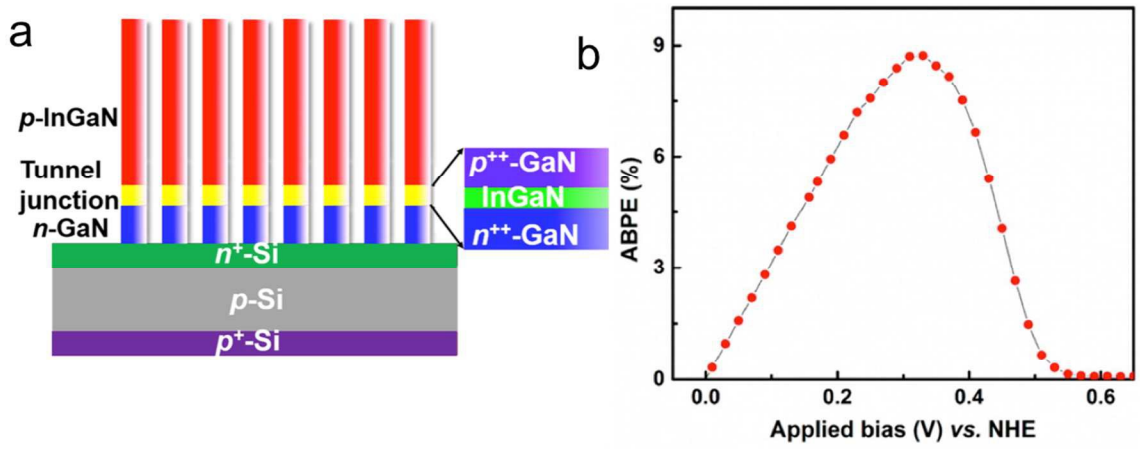

Figure 10: (a) Schematic of the photocathode grown on n^{+}-p Si solar cell substrate. The n-GaN and p-InGaN nanowire segments are connected by an n^{++}-GaN/InGaN/p^{++}-GaN polarization-enhanced tunnel junction, as shown in the inset. (b) Applied-bias-to-photon-conversion-efficiency (ABPE) vs. applied bias (vs. NHE) of the photocathode in 1M HBr electrolyte under 1.3 sun illumination.[196]

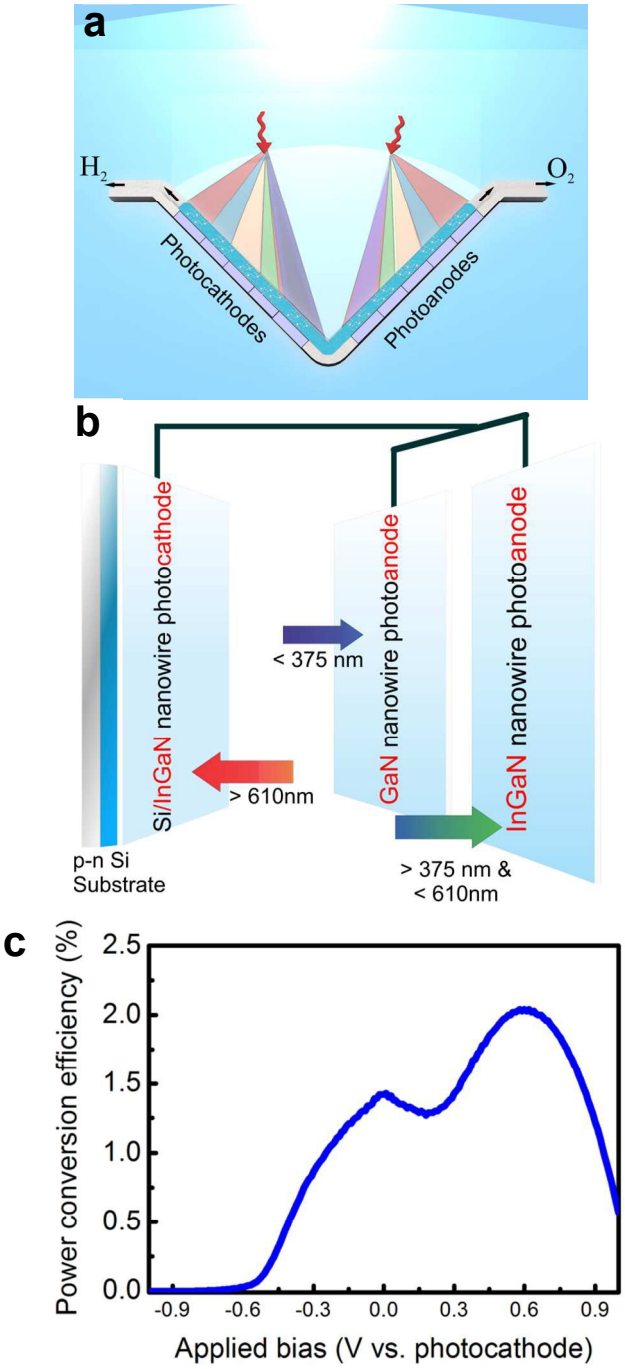

Figure 11: (a) Conceptual view of a dual-photoelectrode system under parallel illumination, in which the incident solar spectrum is spatially and spectrally split on the photoanode and photocathode. The photoanode (or photocathode) may be formed by parallel-connected anodes (or cathodes), each of which is illuminated with certain portion of the solar spectrum. (b) Schematic of parallel-connected GaN and InGaN nanowire photoanode, and Si/InGaN photocathode. The incident sunlight is spectrally and spatially split among the photoelectrodes. (c) The power conversion efficiency of the dual-photoelectrode device (as shown in b) vs. applied bias under AM1.5G 1 sun illumination. The maximum power conversion efficiency is estimated to be ~ 2% at ~ 0.6 V vs. photocathode.[197]

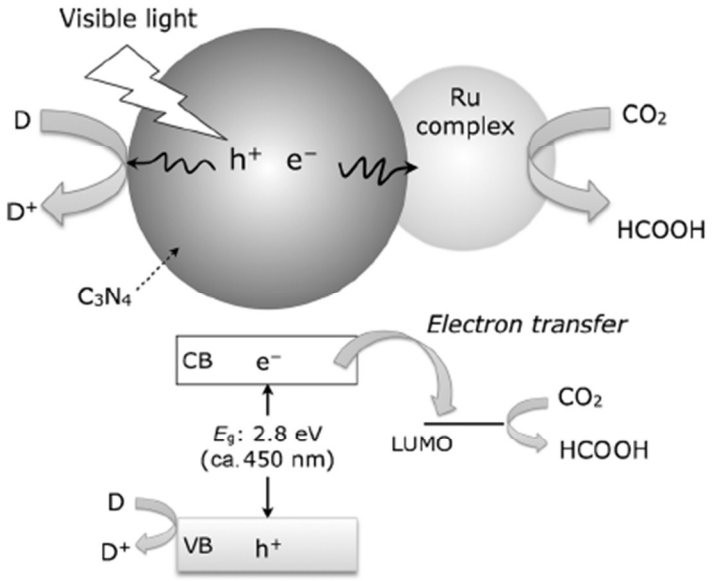

Figure 12: Schematic of photochemical CO_2 reduction to HCOOH using a Ru complex/C_3N_4 hybrid photocatalyst.[207]

References

1. N. S. Lewis and D. G. Nocera, *Proc. Natl. Acad. Sci.* 2006, **103**, 15729-15735.
2. M. A. Green, K. Emery, Y. Hishikawa, W. Warta and E. D. Dunlop, *Prog. Photovoltaics*, 2015, **23**, 1-9.
3. T. R. Cook, D. K. Dogutan, S. Y. Reece, Y. Surendranath, T. S. Teets and D. G. Nocera, *Chem. Rev.*, 2010, **110**, 6474-6502.
4. D. G. Nocera, *Acc. Chem. Res.*, 2012, **45**, 767-776.
5. Y. Tachibana, L. Vayssieres and J. R. Durrant, *Nat. Photon.*, 2012, **6**, 511-518.
6. A. J. Bard and M. A. Fox, *Acc. Chem. Res*, 1995, **28**, 141-145.
7. M. Graetzel, *Acc. Chem. Res*, 1981, **14**, 376-384.
8. R. L. House, N. Y. M. Iha, R. L. Coppo, L. Alibabaei, B. D. Sherman, P. Kang, M. K. Brennaman, P. G. Hoertz and T. J. Meyer, *J. Photochem. Photobiol. C: Photochem. Rev*, 2015. DOI:10.1016/j.jphotochemrev.2015.08.002
9. S. Bensaid, G. Centi, E. Garrone, S. Perathoner and G. Saracco, *ChemSusChem*, 2012, **5**, 500-521.
10. X. Li, J. G. Yu, J. X. Low, Y. P. Fang, J. Xiao and X. B. Chen, *J. Mater. Chem. A*, 2015, **3**, 2485-2534.
11. X. Chen, S. Shen, L. Guo and S. S. Mao, *Chem. Rev.*, 2010, **110**, 6503-6570.
12. J. A. Turner, *Science*, 1999, **285**, 687-689.
13. J. A. Turner, *Science*, 2004, **305**, 972-974.
14. A. Goeppert, M. Czaun, J. P. Jones, G. K. S. Prakash and G. A. Olah, *Chem. Soc. Rev.*, 2014, **43**, 7995-8048.
15. J. Mao, K. Li and T. Peng, *Catal. Sci. Tech*, 2013, **3**, 2481-2498.
16. L. Yuan and Y. J. Xu, *Appl. Surf. Sci*, 2015, **342**, 154-167.
17. G. Ciamician, *Science*, 1912, **36**, 385-394.
18. P. Boddy, *J. Electrochem. Soc.*, 1968, **115**, 199-203.
19. A. Fujishima and K. Honda, *Nature*, 1972, **238**, 37-38.
20. M. Halmann, *Nature*, 1978, **275**, 115-116.
21. T. Inoue, A. Fujishima, S. Konishi and K. Honda, *Nature*, 1979, **277**, 637-638.
22. A. J. Bard, *J. Photochem.*, 1979, **10**, 59-75.
23. J. R. Bolton, S. J. Strickler and J. S. Connolly, *Nature*, 1985, **316**, 495-500.
24. B. A. Pinaud, J. D. Benck, L. C. Seitz, A. J. Forman, Z. B. Chen, T. G. Deutsch, B. D. James, K. N. Baum, G. N. Baum, S. Ardo, H. L. Wang, E. Miller and T. F. Jaramillo, *Energy Environ. Sci*, 2013, **6**, 1983-2002.
25. A. Kudo and Y. Miseki, *Chem. Soc. Rev.*, 2009, **38**, 253-278.
26. L. Vayssieres, *On Solar Hydrogen and Nanotechnology*, John Wiley & Sons, 2010.
27. R. Asahi, T. Morikawa, T. Ohwaki, K. Aoki and Y. Taga, *Science*, 2001, **293**, 269-271.
28. X. Chen, L. Liu, P. Y. Yu and S. S. Mao, *Science*, 2011, **331**, 746-750.
29. K. Maeda, K. Teramura, D. Lu, T. Takata, N. Saito, Y. Inoue and K. Domen, *Nature*, 2006, **440**, 295-295.
30. S. Linic, P. Christopher and D. B. Ingram, *Nat. Mater.*, 2011, **10**, 911-921.
31. J. Q. Chen, D. H. Yang, D. Song, J. H. Jiang, A. B. Ma, M. Z. Hu and C. Y. Ni, *J. Power Sources*, 2015, **280**, 649-666.
32. L. Liao, Q. Zhang, Z. Su, Z. Zhao, Y. Wang, Y. Li, X. Lu, D. Wei, G. Feng, Q. Yu, X. Cai, J. Zhao, Z. Ren, H. Fang, F. Robles-Hernandez, S. Baldelli and J. Bao, *Nat. Nano.*, 2014, **9**, 69-73.
33. J. Liu, Y. Liu, N. Y. Liu, Y. Z. Han, X. Zhang, H. Huang, Y. Lifshitz, S. T. Lee, J. Zhong and Z. H. Kang, *Science*, 2015, **347**, 970-974.
34. M. G. Kibria, F. A. Chowdhury, S. Zhao, B. AlOtaibi, M. L. Trudeau, H. Guo and Z. Mi, *Nat. Commun.*, 2015, **6**.
35. A. Kudo, *Mrs Bull*, 2011, **36**, 32-38.
36. K. Maeda, *ACS Catal.*, 2013, **3**, 1486-1503.
37. R. Abe, *J. Photochem. Photobiol. C: Photochem. Rev.*, 2010, **11**, 179-209.
38. H. Kato, Y. Sasaki, N. Shirakura and A. Kudo, *J. Mater. Chem. A*, 2013, **1**, 12327-12333.
39. M. G. Walter, E. L. Warren, J. R. McKone, S. W. Boettcher, Q. Mi, E. A. Santori and N. S. Lewis, *Chem. Rev.*, 2010, **110**, 6446-6473.
40. F. E. Osterloh, *Top. Curr. Chem*. Springer, 2015, 1-38.
41. R. Marschall, *Adv. Func. Mater.*, 2014, 2014, **24**, 2421-2440.
42. S. Licht, *J. Phys. Chem. B*, 2001, **105**, 6281-6294.

43. O. Khaselev and J. A. Turner, *Science*, 1998, **280**, 425-427.
44. J. S. Luo, J. H. Im, M. T. Mayer, M. Schreier, M. K. Nazeeruddin, N. G. Park, S. D. Tilley, H. J. Fan and M. Gratzel, *Science*, 2014, **345**, 1593-1596.
45. F. F. Abdi, L. Han, A. H. M. Smets, M. Zeman, B. Dam and R. van de Krol, *Nat. Commun.*, 2013, **4**.
46. S. Y. Reece, J. A. Hamel, K. Sung, T. D. Jarvi, A. J. Esswein, J. J. H. Pijpers and D. G. Nocera, *Science*, 2011, **334**, 645-648.
47. J. Brillet, J.-H. Yum, M. Cornuz, T. Hisatomi, R. Solarska, J. Augustynski, M. Graetzel and K. Sivula, *Nat. Photon.*, 2012, **6**, 824-828.
48. S. A. Bonke, M. Wiechen, D. R. MacFarlane and L. Spiccia, *Energy Environ. Sci.*, 2015, **8**, 2791-2796.
49. C. R. Cox, J. Z. Lee, D. G. Nocera and T. Buonassisi, *Proc. Natl. Acad. Sci*., 2014, **111**, 14057-14061.
50. K. Fujii, S. Nakamura, M. Sugiyama, K. Watanabe, B. Bagheri and Y. Nakano, *Int. J. Hydrogen Energy*, 2013, **38**, 14424-14432.
51. G. Peharz, F. Dimroth and U. Wittstadt, *Int. J. Hydrogen Energy*, 2007, **32**, 3248-3252.
52. O. Khaselev, A. Bansal and J. A. Turner, *Int. J. Hydrogen Energy*, 2001, **26**, 127-132.
53. R. E. Blankenship, D. M. Tiede, J. Barber, G. W. Brudvig, G. Fleming, M. Ghirardi, M. R. Gunner, W. Junge, D. M. Kramer, A. Melis, T. A. Moore, C. C. Moser, D. G. Nocera, A. J. Nozik, D. R. Ort, W. W. Parson, R. C. Prince and R. T. Sayre, *Science*, 2011, **332**, 805-809.
54. O. K. Varghese and C. A. Grimes, *Sol. Energy Mater. Sol. Cells*, 2008, **92**, 374-384.
55. H. Gerischer, *Faraday Discuss. Chem. Soc*, 1980, **70**, 137-151.
56. S. Hu, M. R. Shaner, J. A. Beardslee, M. Lichterman, B. S. Brunschwig and N. S. Lewis, *Science*, 2014, **344**, 1005-1009.
57. M. J. Kenney, M. Gong, Y. Li, J. Z. Wu, J. Feng, M. Lanza and H. Dai, *Science*, 2013, **342**, 836-840.
58. N. C. Strandwitz, D. J. Comstock, R. L. Grimm, A. C. Nichols-Nielander, J. Elam and N. S. Lewis, *J. Phys. Chem. C*, 2013, **117**, 4931-4936.
59. Y. W. Chen, J. D. Prange, S. Dühnen, Y. Park, M. Gunji, C. E. D. Chidsey and P. C. McIntyre, *Nat. Mater.*, 2011, **10**, 539-544.
60. L. Ji, M. D. McDaniel, S. Wang, A. B. Posadas, X. Li, H. Huang, J. C. Lee, A. A. Demkov, A. J. Bard, J. G. Ekerdt and E. T. Yu, *Nat. Nanotechnol.*, 2015, **10**, 84-90.
61. Y. Nanishi, *Nat. Photon.*, 2014, **8**, 884-886.
62. K. Domen, *Electrochem. Soc. Interface*, 2013, 57-62.
63. K. Maeda and K. Domen, *J. Phys. Chem. C*, 2007, **111**, 7851-7861.
64. S. Arafin, X. H. Liu and Z. T. Mi, *J. Nanophoton.*, 2013, **7**.
65. J. Wu, *J. Appl. Phys.*, 2009, **106**, 011101.
66. P. G. Moses and C. G. V. d. Walle, *Appl. Phys. Lett.*, 2010, **96**, 021908.
67. A. G. Bhuiyan, A. Hashimoto and A. Yamamoto, *J. Appl. Phys.*, 2003, **94**, 2779-2808.
68. O. Ambacher, *J. Phys. D: Appl. Phys*, 1998, **31**, 2653.
69. T. D. Moustakas, *Phys. Status Solidi A*, 2013, **210**, 169-174.
70. B. AlOtaibi, H. P. T. Nguyen, S. Zhao, M. G. Kibria, S. Fan and Z. Mi, *Nano Lett.*, 2013, **13**, 4356-4361.
71. H. S. Jung, Y. J. Hong, Y. Li, J. Cho, Y.-J. Kim and G.-C. Yi, *ACS Nano*, 2008, **2**, 637-642.
72. D. Zhuang and J. H. Edgar, *Mater. Sci. Eng., R*, 2005, **48**, 1-46.
73. F. E. Osterloh, *Chem. Soc. Rev.*, 2013, **42**, 2294-2320.
74. S. S. Kocha, M. W. Peterson, D. J. Arent, J. M. Redwing, M. A. Tischler and J. A. Turner, *J. Electrochem. Soc.*, 1995, **142**, L238-L240.
75. J. Beach, R. Collins and J. Turner, *J. Electrochem. Soc.*, 2003, **150**, A899-A904.
76. K. Fujii, T. Karasawa and K. Ohkawa, *Jpn. J. Appl. Phys*, 2005, **44**, L543.
77. K. Fujii and K. Ohkawa, *Jpn. J. Appl. Phys*, 2005, **44**, L909.
78. K. Fujii and K. Ohkawa, *Phys. Status Solidi C*, 2006, **3**, 2270-2273.
79. K. Fujii and K. Ohkawa, *J. Electrochem. Soc*, 2006, **153**, A468-A471.
80. X. Wang, K. Maeda, A. Thomas, K. Takanabe, G. Xin, J. M. Carlsson, K. Domen and M. Antonietti, *Nat. Mater.*, 2009, **8**, 76-80.
81. Q. Huang, Z. Ye and X. Xiao, *J. Mater. Chem. A*, 2015, **3**, 15824-15837.
82. S. Bai, J. Jiang, Q. Zhang and Y. J. Xiong, *Chem. Soc. Rev.*, 2015, **44**, 2893-2939.

83. A. Kudo, *Int. J. Hydrogen Energy*, 2007, **32**, 2673-2678.
84. H. Tong, S. Ouyang, Y. Bi, N. Umezawa, M. Oshikiri and J. Ye, *Adv. Mater.*, 2012, **24**, 229-251.
85. X. Chen, C. Li, M. Graetzel, R. Kostecki and S. S. Mao, *Chem. Soc. Rev.*, 2012, **41**, 7909-7937.
86. L. Yang, H. Zhou, T. Fan and D. Zhang, *Phys. Chem. Chem.Phys.*, 2014, **16**, 6810-6826.
87. J. Tang, J. R. Durrant and D. R. Klug, *J. Am. Chem. Soc.*, 2008, **130**, 13885-13891.
88. J. Yang, D. Wang, H. Han and C. Li, *Acc. Chem. Res*, 2013, **46**, 1900-1909.
89. W.-F. Chen, K. Sasaki, C. Ma, A. I. Frenkel, N. Marinkovic, J. T. Muckerman, Y. Zhu and R. R. Adzic, *Angew. Chem. Int. Ed*, 2012, **51**, 6131-6135.
90. M. Shalom, D. Ressnig, X. Yang, G. Clavel, T. P. Fellinger and M. Antonietti, *J. Mater. Chem. A*, 2015, **3**, 8171-8177.
91. B. Cao, G. M. Veith, J. C. Neuefeind, R. R. Adzic and P. G. Khalifah, *J. Am. Chem. Soc.*, 2013, **135**, 19186-19192.
92. H. X. Zhong, H. M. Zhang, Y. M. Liang, J. L. Zhang, M. R. Wang and X. L. Wang, *J. Power Sources*, 2007, **164**, 572-577.
93. J. Sato, N. Saito, Y. Yamada, K. Maeda, T. Takata, J. N. Kondo, M. Hara, H. Kobayashi, K. Domen and Y. Inoue, *J. Am. Chem. Soc.*, 2005, **127**, 4150-4151.
94. K. Maeda, N. Saito, D. Lu, Y. Inoue and K. Domen, *J. Phys. Chem. C*, 2007, **111**, 4749-4755.
95. Y. Lee, T. Watanabe, T. Takata, M. Hara, M. Yoshimura and K. Domen, *J. Phys. Chem. B*, 2006, **110**, 17563-17569.
96. N. Arai, N. Saito, H. Nishiyama, Y. Inoue, K. Domen and K. Sato, *Chem. Lett.*, 2006, **35**, 796-797.
97. T. Kida, Y. Minami, G. Guan, M. Nagano, M. Akiyama and A. Yoshida, *J. Mater. Sci.* 2006, **41**, 3527-3534.
98. N. Arai, N. Saito, H. Nishiyama, K. Domen, H. Kobayashi, K. Sato and Y. Inoue, *Catal. Today*, 2007, **129**, 407-413.
99. K. Maeda, K. Teramura, N. Saito, Y. Inoue and K. Domen, *Bull. Chem. Soc. Jpn*, 2007, **80**, 1004-1010.
100. A. Kubacka, M. Fernandez-Garcia and G. Colon, *Chem. Rev.*, 2011, **112**, 1555-1614.
101. D. Wang, A. Pierre, M. G. Kibria, K. Cui, X. Han, K. H. Bevan, H. Guo, S. Paradis, A.-R. Hakima and Z. Mi, *Nano Lett.*, 2011, **11**, 2353-2357.
102. X. Shen, Y. A. Small, J. Wang, P. B. Allen, M. V. Fernandez-Serra, M. S. Hybertsen and J. T. Muckerman, *J. Phys. Chem. C*, 2010, **114**, 13695-13704.
103. X. Shen, P. B. Allen, M. S. Hybertsen and J. T. Muckerman, *J. Phys. Chem. C*, 2009, **113**, 3365-3368.
104. U. Aschauer, Y. He, H. Cheng, S.-C. Li, U. Diebold and A. Selloni, *J. Phys. Chem. C*, 2010, **114**, 1278-1284.
105. U. Diebold, N. Ruzycki, G. S. Herman and A. Selloni, *Catal. Today*, 2003, **85**, 93-100.
106. A. Vittadini, A. Selloni, F. P. Rotzinger and M. Gratzel, *Phys. Rev. Lett.*, 1998, **81**, 2954-2957.
107. J. Wang, L. S. Pedroza, A. Poissier and M. V. Fernández-Serra, *J. Phys. Chem. C*, 2012, **116**, 14382-14389.
108. K. Maeda, K. Teramura and K. Domen, *J. Catal.*, 2008, **254**, 198-204.
109. Y. Li, L. Zhu, Y. Yang, H. Song, Z. Lou, Y. Guo and Z. Ye, *Small*, 2015, **11**, 871-876.
110. M. G. Kibria, F. A. Chowdhury, S. Zhao, M. L. Trudeau, H. Guo and Z. Mi, *Appl. Phys. Lett*, 2015, **106,** 113105.
111. T. Stoica and R. Calarco, *IEEE J. Sel. Topics Quantum Electron.*, 2011, **17**, 859-868.
112. F. Yam and Z. Hassan, *Superlattices Microstruct.*, 2008, **43**, 1-23.
113. I. h. Ho and G. B. Stringfellow, *Appl. Phys. Lett*, 1996, **69**, 2701-2703.
114. M. Li, W. Luo, B. Liu, X. Zhao, Z. Li, D. Chen, T. Yu, Z. Xie, R. Zhang and Z. Zou, *Appl. Phys. Lett*, 2011, **99**, 112108
115. W. Lü, D. B. Li, C. R. Li, F. Shen and Z. Zhang, *J. Appl. Phys*, 2004, **95**, 4362-4366.
116. R. Singh, D. Doppalapudi, T. Moustakas and L. Romano, *Appl. Phys. Lett.*, 1997, **70**, 1089-1091.
117. Z. Mi and S. Zhao, *Phys. Status Solidi B*, 2015, **252**, 1050-1062.
118. M. G. Kibria, H. P. T. Nguyen, K. Cui, S. Zhao, D. Liu, H. Guo, M. L. Trudeau, S. Paradis, A.-R. Hakima and Z. Mi, *ACS Nano*, 2013, **7**, 7886-7893.
119. M. Kibria, F. Chowdhury, M. Trudeau, H. Guo and Z. Mi, *Nanotechnol.*, 2015, **26**, 285401.
120. G. Hitoki, A. Ishikawa, T. Takata, J. N. Kondo, M. Hara and K. Domen, *Chem. Lett.*, 2002, 736-737.
121. W.-J. Chun, A. Ishikawa, H. Fujisawa, T. Takata, J. N. Kondo, M. Hara, M. Kawai, Y. Matsumoto and K. Domen, *J. Phys. Chem B*, 2003, **107**, 1798-1803.
122. M. Tabata, K. Maeda, M. Higashi, D. Lu, T. Takata, R. Abe and K. Domen, *Langmuir*, 2010, **26**, 9161-9165.
123. P. Zhang, J. Zhang and J. Gong, *Chem. Soc. Rev.*, 2014, **43**, 4395-4422.

124. S. S. K. Ma, T. Hisatomi, K. Maeda, Y. Moriya and K. Domen, *J. Am. Chem. Soc*, 2012, **134**, 19993-19996.
125. S. Chen, S. Shen, G. Liu, Y. Qi, F. Zhang and C. Li, *Angew. Chem. Int. Ed.*, 2015, **54**, 3047-3051.
126. S. W. Cao, J. X. Low, J. G. Yu and M. Jaroniec, *Adv. Mater*, 2015, **27**, 2150-2176.
127. Y. Zheng, L. Lin, B. Wang and X. Wang, *Angew. Chem. Int. Ed.*, 2015, **54**, 12868-12884.
128. X. Wang, S. Blechert and M. Antonietti, *ACS Catal.*, 2012, **2**, 1596-1606.
129. J. Zhang, Y. Chen and X. Wang, *Energy Environ. Sci.*, 2015,**8**, 3092-3108
130. Y. Cui, J. Huang, X. Fu and X. Wang, *Catal. Sci. Tech.*, 2012, **2**, 1396-1402.
131. J. Zhang, F. Guo and X. Wang, *Adv. Funct. Mater.*, 2013, **23**, 3008-3014.
132. J. Zhang, M. Zhang, C. Yang and X. Wang, *Adv. Mater.*, 2014, **26**, 4121-4126.
133. J. Sun, J. Zhang, M. Zhang, M. Antonietti, X. Fu and X. Wang, *Nat. Commun.*, 2012, 1139.
134. Y. Zheng, L. Lin, X. Ye, F. Guo and X. Wang, *Angew. Chem. Int. Ed.*, 2014, **53**, 11926-11930.
135. Y. Cui, Z. Ding, X. Fu and X. Wang, *Angew. Chem. Int. Ed.*, 2012, **51**, 11814-11818.
136. Z. Hong, B. Shen, Y. Chen, B. Lin and B. Gao, *J. Mater. Chem. A*, 2013, **1**, 11754-11761.
137. Y. Wang, Y. Di, M. Antonietti, H. Li, X. Chen and X. Wang, *Chem. Mater.*, 2010, **22**, 5119-5121.
138. G. Zhang, M. Zhang, X. Ye, X. Qiu, S. Lin and X. Wang, *Adv. Mater.*, 2014, **26**, 805-809.
139. X. Wang, X. Chen, A. Thomas, X. Fu and M. Antonietti, *Adv. Mater.*, 2009, **21**, 1609-1612.
140. Z. Ding, X. Chen, M. Antonietti and X. Wang, *ChemSusChem*, 2011, **4**, 274-281.
141. M. Zhang and X. Wang, *Energy Environ. Sci.*, 2014, **7**, 1902-1906.
142. J. Zhang, M. Zhang, S. Lin, X. Fu and X. Wang, *J. Catal.*, 2014, **310**, 24-30.
143. K. Takanabe, K. Kamata, X. Wang, M. Antonietti, J. Kubota and K. Domen, *Phys. Chem. Chem. Phys.*, 2010, **12**, 13020-13025.
144. Y. Hou, A. B. Laursen, J. Zhang, G. Zhang, Y. Zhu, X. Wang, S. Dahl and I. Chorkendorff, *Angew. Chem. Int. Ed.*, 2013, **52**, 3621-3625.
145. A. Du, S. Sanvito, Z. Li, D. Wang, Y. Jiao, T. Liao, Q. Sun, Y. H. Ng, Z. Zhu, R. Amal and S. C. Smith, *J. Am. Chem. Soc.*, 2012, **134**, 4393-4397.
146. L. Ge and C. Han, *Appl. Catal. B: Environmental*, 2012, **117–118**, 268-274.
147. J. Yu, S. Wang, B. Cheng, Z. Lin and F. Huang, *Catal. Sci. Technol.*, 2013, **3**, 1782-1789.
148. L. Yin, Y.-P. Yuan, S.-W. Cao, Z. Zhang and C. Xue, *RSC Adv.*, 2014, **4**, 6127-6132.
149. G. Zhang, S. Zang, Z.-A. Lan, C. Huang, G. Li and X. Wang, *J. Mater. Chem. A*, 2015, **3**, 17946-17950.
150. D. J. Martin, K. Qiu, S. A. Shevlin, A. D. Handoko, X. Chen, Z. Guo and J. Tang, *Angew. Chem. Int. Ed*, 2014, **53**, 9240-9245.
151. Q. Xiang, J. Yu and M. Jaroniec, *J. Phys. Chem. C*, 2011, **115**, 7355-7363.
152. J. Sun, J. Zhang, M. Zhang, M. Antonietti, X. Fu and X. Wang, *Nat. Commun.*, 2012, 1139.
153. Y. Wang, J. Hong, W. Zhang and R. Xu, *Catal. Sci. Technol.*, 2013, **3**, 1703-1711.
154. C. Huang, C. Chen, M. Zhang, L. Lin, X. Ye, S. Lin, M. Antonietti and X. Wang, *Nat. Commun.*, 2015, **6**.
155. M. G. Kibria, S. Zhao, F. A. Chowdhury, Q. Wang, H. P. T. Nguyen, M. L. Trudeau, H. Guo and Z. Mi, *Nat. commun.*, 2014, **5**.
156. Z. Zhang and J. T. Yates, *Chem. Rev.*, 2012, **112**, 5520-5551.
157. F. A. Chowdhury, Z. Mi, M. G. Kibria and M. L. Trudeau, *APL Mater.*, 2015, **3**, 104408.
158. Y.-C. Pu, M. G. Kibria, Z. Mi and J. Z. Zhang, *J. Phys. Chem. Lett.*, 2015, **6**, 2649-2656.
159. M. Ono, K. Fujii, T. Ito, Y. Iwaki, A. Hirako, T. Yao and K. Ohkawa, *J. Phys. Chem. Lett.*, 2007, **126**, -.
160. K. Fujii, H. Nakayama, K. Sato, T. Kato, M.-W. Cho and T. Yao, *Phys. Status Solidi C*, 2008, **5**, 2333-2335.
161. I. Waki, D. Cohen, R. Lal, U. Mishra, S. P. DenBaars and S. Nakamura, *Appl. Phys. Lett*, 2007, **91**, 093519.
162. S.-Y. Liu, Y.-C. Lin, J.-C. Ye, S. Tu, F. Huang, M. Lee, W. Lai and J. Sheu, *Opt. Express*, 2011, **19**, A1196-A1201.
163. S.-Y. Liu, J. Sheu, M. Lee, Y.-C. Lin, S. Tu, F. Huang and W. Lai, *Opt. Express*, 2012, **20**, A190-A196.
164. S. Kikawa, N. Kobayashi, J. Yamamoto, Y. Ban and K. Matsumoto, *J. Surface Sci. Nanotech.*, 2009, **7**, 847-850.
165. Y.-G. Lin, Y.-K. Hsu, A. M. Basilio, Y.-T. Chen, K.-H. Chen and L.-C. Chen, *Opt. Express*, 2014, **22**, A21-A27.
166. A. Nakamura, K. Fujii, M. Sugiyama and Y. Nakano, *Phys. Chem. Chem. Phys*, 2014, **16**, 15326-15330.
167. J. Benton, J. Bai and T. Wang, *Appl. Phys. Lett.*, 2013, **102**, 173905.
168. B. AlOtaibi, M. Harati, S. Fan, S. Zhao, H. Nguyen, M. Kibria and Z. Mi, *Nanotechnol.*, 2013, **24**, 175401.
169. J. Wallys, S. Hoffmann, F. Furtmayr, J. Teubert and M. Eickhoff, *Nanotechnol.*, 2012, **23**, 165701.
170. S.-Y. Liu, J. Sheu, Y.-C. Lin, S. Tu, F. Huang, M. Lee and W. Lai, *Opt. Express*, 2012, **20**, A678-A683.

171. K. Fujii, K. Kusakabe and K. Ohkawa, *Jpn. J. Appl. Phys*, 2005, **44**, 7433.
172. J. Li, J. Y. Lin and H. X. Jiang, *Appl. Phys. Lett* 2008, **93**, 162107-162107-162103.
173. K. Aryal, B. N. Pantha, J. Li, J. Y. Lin and H. X. Jiang, *Appl. Phys. Lett*, 2010, **96**, 052110.
174. W. Luo, B. Liu, Z. Li, Z. Xie, D. Chen, Z. Zou and R. Zhang, *Appl. Phys. Lett*, 2008, **92**, 262110.
175. M. Li, W. Luo, Q. Liu, Z. Zhuang, Z. Li, B. Liu, D. Chen, R. Zhang, T. Yu and Z. Zou, *J. Phys. D: Appl. Phys*, 2013, **46**, 345103.
176. N. H. Alvi, P. E. D. Soto Rodriguez, P. Kumar, V. J. Gómez, P. Aseev, A. H. Alvi, M. A. Alvi, M. Willander and R. Nötzel, *Appl. Phys. Lett.*, 2014, **104**, 223104.
177. J. Benton, J. Bai and T. Wang, *Appl. Phys. Lett.*, 2014, **105,** 223902.
178. Y. J. Hwang, C. H. Wu, C. Hahn, H. E. Jeong and P. Yang, *Nano Lett.*, 2012, **12**, 1678-1682.
179. L. Caccamo, J. Hartmann, C. Fàbrega, S. Estradé, G. Lilienkamp, J. D. Prades, M. W. Hoffmann, J. Ledig, A. Wagner and X. Wang, *ACS Appl. Mater Interf.*, 2014, **6**, 2235-2240.
180. M. Ebaid, J.-H. Kang, S.-H. Lim, J.-S. Ha, J. K. Lee, Y.-H. Cho and S.-W. Ryu, *Nano Energy*, 2015, **12**, 215-223.
181. M. Ebaid, J.-H. Kang, S.-H. Lim, Y.-H. Cho and S.-W. Ryu, *RSC Adv.*, 2015, **5**, 23303-23310.
182. J. Kamimura, P. Bogdanoff, J. Lähnemann, C. Hauswald, L. Geelhaar, S. Fiechter and H. Riechert, *J. Am. Chem. Soc.*, 2013, **135**, 10242-10245.
183. J. Benton, J. Bai and T. Wang, *Appl. Phys. Lett.*, 2013, **103**, 133904.
184. P. E. D. S. Rodriguez, P. Aseev, V. J. Gómez, W. ul Hassan, M. Willander and R. Nötzel, *Nano Energy*, 2015, **13**, 291-297.
185. S. Rajaambal, M. Mapa and C. S. Gopinath, *Dalton Trans.*, 2014, **43**, 12546-12554.
186. V. Chakrapani, J. Thangala and M. K. Sunkara, *Int. J. Hydrogen Energy,* 2009, **34**, 9050-9059.
187. X. Feng, T. J. LaTempa, J. I. Basham, G. K. Mor, O. K. Varghese and C. A. Grimes, *Nano lett.*, 2010, **10**, 948-952.
188. Y. Cong, H. S. Park, S. Wang, H. X. Dang, F.-R. F. Fan, C. B. Mullins and A. J. Bard, *J. Phys. Chem.*, 2012, **116**, 14541-14550.
189. M. Higashi, K. Domen and R. Abe, *Energy Environ. Sci.*, 2011, **4**, 4138-4147.
190. M. Li, W. Luo, D. Cao, X. Zhao, Z. Li, T. Yu and Z. Zou, *Angew. Chem. Int. Ed.*, 2013, **52**, 11016-11020.
191. G. Liu, J. Shi, F. Zhang, Z. Chen, J. Han, C. Ding, S. Chen, Z. Wang, H. Han and C. Li, *Angew. Chem.*, 2014, **126**, 7295-7299.
192. Y. Li, T. Takata, D. Cha, K. Takanabe, T. Minegishi, J. Kubota and K. Domen, *Adv. Mater.*, 2013, **25**, 125-131.
193. J. Hou, Z. Wang, C. Yang, H. Cheng, S. Jiao and H. Zhu, *Energy Environ. Sci*, 2013, **6**, 3322-3330.
194. M. Liao, J. Feng, W. Luo, Z. Wang, J. Zhang, Z. Li, T. Yu and Z. Zou, *Adv. Func. Mater.*, 2012, **22**, 3066-3074.
195. S.-Y. Liu, J. Sheu, Y.-C. Lin, Y.-T. Chen, S. Tu, M. Lee and W. Lai, *Opt. Express*, 2013, **21**, A991-A996.
196. R. Dahal, B. N. Pantha, J. Li, J. Y. Lin and H. X. Jiang, *Appl. Phys. Lett.*, 2014, **104**, 143901.
197. S. Fan, B. AlOtaibi, S. Y. Woo, Y. Wang, G. A. Botton and Z. Mi, *Nano Lett.*, 2015, **15**, 2721-2726.
198. B. AlOtaibi, S. Fan, S. Vanka, M. G. Kibria and Z. Mi, *Nano Lett.*, 2015, **15**, 6821-6828.
199. B. AlOtaibi, S. Fan, D. Wang, J. Ye and Z. Mi, 2015, **5**, 5342–5348.
200. S. Yotsuhashi, M. Deguchi, Y. Zenitani, R. Hinogami, H. Hashiba, Y. Yamada and K. Ohkawa, *Appl. Phys. Exp.*, 2011, **4**, 117101.
201. S. Yotsuhashi, M. Deguchi, Y. Zenitani, R. Hinogami, H. Hashiba, Y. Yamada and K. Ohkawa, *Jpn. J. Appl. Phys.*, 2012, **51**, 02BP07.
202. S. Yotsuhashi, M. Deguchi, H. Hashiba, Y. Zenitani, R. Hinogami, Y. Yamada and K. Ohkawa, *Appl. Phys. Lett.*, 2012, **100**, 243904.
203. S. Yotsuhashi, H. Hashiba, M. Deguchi, Y. Zenitani, R. Hinogami, Y. Yamada, M. Deura and K. Ohkawa, *AIP Adv.*, 2012, **2**, 042160.
204. T. Sekimoto, S. Shinagawa, Y. Uetake, K. Noda, M. Deguchi, S. Yotsuhashi and K. Ohkawa, *Appl. Phys. Lett.*, 2015, **106**, 073902.
205. R. Kuriki, K. Sekizawa, O. Ishitani and K. Maeda, *Angew. Chem. Int. Ed*, 2015, **54**, 2406-2409.
206. J. Lin, Z. Pan and X. Wang, *ACS Sustainable Chem. Eng*, 2014, **2**, 353-358.
207. K. Maeda, R. Kuriki, M. Zhang, X. Wang and O. Ishitani, *J. Mater. Chem. A*, 2014, **2**, 15146-15151.
208. K. Maeda, K. Sekizawa and O. Ishitani, *Chem. Commun.*, 2013, **49**, 10127-10129.
209. J. Mao, T. Peng, X. Zhang, K. Li, L. Ye and L. Zan, *Catal. Sci. Tech.*, 2013, **3**, 1253-1260.
210. T. Ohno, N. Murakami, T. Koyanagi and Y. Yang, *J. of CO_2 Util*, 2014, **6**, 17-25.

211. J. Qin, S. Wang, H. Ren, Y. Hou and X. Wang, *Appl. Catal. B: Env.*, 2015, **179**, 1-8.
212. G. Dong and L. Zhang, *J. Mater. Chem.*, 2012, **22**, 1160-1166.
213. J. Yu, K. Wang, W. Xiao and B. Cheng, *Phys. Chem. Chem. Phys.*, 2014, **16**, 11492-11501.
214. S. Bai, X. Wang, C. Hu, M. Xie, J. Jiang and Y. Xiong, *Chem. Commun.*, 2014, **50**, 6094-6097.
215. S.-W. Cao, X.-F. Liu, Y.-P. Yuan, Z.-Y. Zhang, Y.-S. Liao, J. Fang, S. C. J. Loo, T. C. Sum and C. Xue, *Appl. Catal. B: Env.*, 2014, **147**, 940-946.
216. Y.-P. Yuan, S.-W. Cao, Y.-S. Liao, L.-S. Yin and C. Xue, *Appl. Catal. B: Env.*, 2013, **140–141**, 164-168.
217. DOE, Hydrogen Production Technical Team Roadmap, http://www1.eere.energy.gov/vehiclesandfuels/pdfs/program/hptt_roadmap_june2013.pdf).
218. V. Sukhovatkin, S. Hinds, L. Brzozowski and E. H. Sargent, *Science*, 2009, **324**, 1542-1544.
219. X. Huang, S. Han, W. Huang and X. Liu, *Chem. Soc. Rev.*, 2013, **42**, 173-201.
220. W. Nie, H. Tsai, R. Asadpour, J.-C. Blancon, A. J. Neukirch, G. Gupta, J. J. Crochet, M. Chhowalla, S. Tretiak and M. A. Alam, *Science*, 2015, **347**, 522-525.
221. T. Hamann, *science*, 2014, **1260051**, 345.
222. Q. Dong, Y. Fang, Y. Shao, P. Mulligan, J. Qiu, L. Cao and J. Huang, *Science*, 2015, **347**, 967-970.